Simulating the chemical enrichment of the intergalactic medium

Wiersma, R.P.C.

CHAPTER 3

Chemical enrichment in cosmological, SPH simulations

Robert P. C. Wiersma, Joop Schaye, Tom Theuns, Claudio Dalla Vecchia, and Luca Tornatore

Monthly Notices of the Royal Astronomical Society, 399, 574, 2009

We present an implementation of stellar evolution and chemical feedback for smoothed particle hydrodynamics (SPH) simulations. We consider the timed release of individual elements by both massive and intermediate mass stars. We contrast two reasonable definitions of the metallicity of a resolution element and find that while they agree for high metallicities, there are large differences at low metallicities. We argue the discrepancy is indicative of the lack of metal mixing caused by the fact that metals are stuck to particles. We argue that since this is a (numerical) sampling problem, solving it using a poorly constrained physical process such as diffusion could have undesired consequences. We demonstrate that the two metallicity definitions result in redshift $z = 0$ stellar masses that can differ by up to a factor of one and a half, because of the sensitivity of the cooling rates to the elemental abundances.

Finally, we use several 512^3 particle simulations to investigate the evolution of the distribution of heavy elements, which we find to be in reasonably good agreement with available observational constraints. We find that by $z = 0$ most of the metals are locked up in stars. The gaseous metals are distributed over a very wide range of gas densities and temperatures. The shock-heated warm-hot intergalactic medium has a relatively high metallicity of $\sim 10^{-1}\,Z_{\odot}$ that evolves only weakly and is therefore an important reservoir of metals. Any census aiming to account for most of the metal mass will have to take a wide variety of objects and structures into account.

3.1 Introduction

Nucleosynthetic processes within stars and supernovae (SNe) change the abundances of elements in the Universe over time. As stars release these elements back into the diffuse interstellar medium (ISM) that surrounds them, subsequent generations of stars are born with different chemical compositions. On larger scales, winds driven out of galaxies by the energy released by dying stars and/or active galactic nuclei modify the composition of the intergalactic medium (IGM) and hence that of future galaxies. The IGM within groups and clusters of galaxies exerts a ram-pressure on their member galaxies as they move along their orbits. This head-wind can be sufficiently strong to strip the ISM from the galaxies, thus mixing the elements that were present in the ISM into the IGM. These and other processes make the (re-)cycling of elements over time through stars, galaxies and diffuse gas a complicated problem that is well-suited for studies using hydrodynamical simulations.

Simulating the exchange of elements between stars, galaxies, and their environments is the subject of this chapter. Specifically, this chapter describes and tests a method to follow the timed release and subsequent spreading of elements by stellar populations formed in cosmological, hydrodynamical simulations.

The elemental abundances of stars, galaxies, and diffuse gas are of great interest for a variety of reasons. First, the dissipation of binding energy by the emission of "cooling" radiation is a fundamental ingredient of models of the formation of both stars and galaxies. Because radiative cooling rates are very sensitive to abundance variations, the rate at which gas can collapse into galaxies is to a large extent determined by its chemical composition. Similarly, the initial mass function (IMF) of stars may well depend on the chemical composition of the gas from which they formed.

Second, knowledge of elemental abundances can give great insight into a variety of key astrophysical processes. For example, the distribution of elements in the IGM provides stringent constraints on models of galactic winds and ram-pressure stripping in clusters. The relative abundances of elements can tell us about the IMF of the stars that produced them. The abundance of alpha elements - which are released on short time-scales through core collapse SNe - relative to iron - most of which is released much later when intermediate mass stars explode as type Ia SNe - tells us about the time-scale on which stars have been formed. On the other hand, the absolute abundances of metals provide us with a measure of the integral of past star formation.

Third, emission and absorption lines of individual elements constitute key diagnostics of physical conditions, such as gas densities, temperatures, radiation fields and dust content. The strengths of said lines depend on a number of factors, but invariably the abundances play an important role.

Fourth, individual lines are the only observable signatures for most of the diffuse gas in the Universe. For example, oxygen lines are the most promising tools to detect the warm-hot IGM that may host a large fraction of the cosmic baryons. To verify this prediction of structure formation in a cold dark matter universe, it is necessary to know the abundance of oxygen in this elusive gas phase.

Clearly, following the timed release of the elements by stars and their subsequent dispersal through space, a collection of processes sometimes referred to as "chemody-

namics", is a critical ingredient of any realistic simulation of the formation and evolution of galaxies. The implementation of chemodynamics into cosmological simulations is a challenging problem, mainly because such models lack the resolution to resolve many of the relevant physical processes and hence require "sub-grid" recipes.

The first study to implement metal enrichment into a Smoothed Particle Hydrodynamics (SPH) code did not distinguish between different elements and only considered enrichment by core collapse SNe in the instantaneous recycling approximation (Steinmetz & Mueller 1994). Since then many authors have implemented more sophisticated recipes for chemodynamics into SPH codes (e.g. Raiteri et al. 1996; Berczik 1999; Mosconi et al. 2001; Kawata 2001; Lia et al. 2002; Kawata & Gibson 2003; Valdarnini 2003; Kobayashi 2004a; Sommer-Larsen et al. 2005; Tornatore et al. 2007; Oppenheimer & Davé 2008), ranging from recipes that distinguish only between SN type Ia and SN type II elements to models that follow large numbers of individual elements released by AGB stars, SNe Ia, SNe II, and the winds from their progenitors. Three-dimensional chemodynamical simulations have so far been used most often for the study of individual objects such as galaxies (e.g. Theis et al. 1992; Raiteri et al. 1996; Berczik 1999; Recchi et al. 2001; Kawata 2001; Kawata & Gibson 2003; Kobayashi 2004a; Mori & Umemura 2006; Governato et al. 2007) and clusters of galaxies (e.g. Lia et al. 2002; Valdarnini 2003; Tornatore et al. 2004; Sommer-Larsen et al. 2005; Romeo et al. 2006; Tornatore et al. 2007; see Borgani et al. 2008 for a review), but in recent years chemodynamical cosmological simulations have also become more common (e.g. Mosconi et al. 2001; Scannapieco et al. 2005; Kobayashi et al. 2007; Oppenheimer & Davé 2008). Note that several recent cosmological works (Scannapieco et al. 2005; Kobayashi et al. 2007; Oppenheimer & Davé 2008) use our hydrodynamical code of choice, namely the SPH code GADGET (Springel 2005), although they use different implementations of chemodynamics, star formation, galactic winds, and radiative cooling.

Here we present a new implementation of chemodynamics that follows the timed release – by AGB stars, SNe Ia, SNe II, and the winds from their progenitors – of the 11 elements that we found in chapter 2 to contribute significantly to the radiative cooling at $T > 10^4$ K. We present a subset of high-resolution cosmological, hydrodynamical simulations taken from the OverWhelmingly Large Simulations (OWLS) project (Schaye et al. 2009) and use them to test the robustness of our prescription to numerical parameters and to make some predictions regarding the large-scale distribution of heavy elements. These simulations include element-by-element cooling, a first for cosmological chemodynamical simulations, and they take the effect of photo-ionization by the UV/X-ray background radiation on the cooling rates into account, which is normally either ignored or included only for hydrogen and helium. While this chapter focuses on a single implementation of the relevant physics, we will present the effects of varying the physical parameters (e.g., stellar IMF, star formation, cooling, feedback from star formation) and make use of a larger fraction of the OWLS data set in chapter 4.

This chapter is organized as follows. The simulations and the prescriptions used for star formation, feedback from star formation, and radiative cooling are summarized in §3.2. In §3.3 we discuss in some detail the ingredients that we take from models of

Table 3.1: Adopted solar abundances.

Element	$n_i/n_{\rm H}$	Mass Fraction
H	1	0.7065
He	0.1	0.2806
C	2.46×10^{-4}	2.07×10^{-3}
N	8.51×10^{-5}	8.36×10^{-4}
O	4.90×10^{-4}	5.49×10^{-3}
Ne	1.00×10^{-4}	1.41×10^{-3}
Mg	3.47×10^{-5}	5.91×10^{-4}
Si	3.47×10^{-5}	6.83×10^{-4}
S	1.86×10^{-5}	4.09×10^{-4}
Ca	2.29×10^{-6}	6.44×10^{-5}
Fe	2.82×10^{-5}	1.10×10^{-3}

stellar evolution or observations, including the IMF, stellar lifetimes, stellar yields, and SN Ia rates. In §3.5 we discuss how we combine all these ingredients to predict the mass released by a simple stellar population as a function of its age and present some results. Our implementation of chemodynamics into SPH is discussed in §3.6. This section also contrasts two possible definitions of elemental abundances in SPH and demonstrates that the choice of definition can be extremely important due to limitations intrinsic to SPH. In §3.7 we use our simulations to address the question "Where are the metals?" and we show how the answer is influenced by the definition of metallicity that is used. Finally, we provide a detailed summary in §3.8 and investigate convergence with the size of the simulation box and with resolution in appendices 3.A and 3.B, respectively.

For the solar abundance we use the metal mass fraction $Z_\odot = 0.0127$, corresponding to the value obtained using the default abundance set of CLOUDY (version 07.02; last described by Ferland et al. 1998). This abundance set (see Table 3.1) combines the abundances of Allende Prieto et al. (2001, 2002) for C and O, Holweger (2001) for N, Ne, Mg, Si, and Fe, and assumes $n_{\rm He}/n_{\rm H} = 0.1$ which is a typical value for nebular with near-solar compositions. Note that much of the literature assumes $Z_\odot = 0.02$, which is 0.2 dex higher than the value used here.

3.2 SIMULATIONS

We performed cosmological, gas-dynamical simulations using a modified version of the N-body Tree-PM, SPH code GADGET III, which is a modified version of the code GADGET II (Springel 2005). Our prescriptions for star formation, for feedback from core collapse supernovae and for radiative cooling and heating are summarized below. Our prescription for stellar evolution, which is the subject of this chapter, is described in detail in the next section.

We use the suite of simulations of varying box sizes and particle numbers listed in Table 3.2 together with the corresponding particle masses and gravitational force

Table 3.2: List of simulations used. The columns give the comoving size of the box L, the total number of particles per component N (dark matter and baryons), the initial baryonic particle mass $m_{\rm b}$, the dark matter particle mass $m_{\rm dm}$, the (Plummer-equivalent) comoving softening length $\epsilon_{\rm com}$, the maximum (Plummer-equivalent) proper softening length $\epsilon_{\rm prop}$, and the redshift at which the simulation was stopped $z_{\rm end}$.

Simulation	L	N	$m_{\rm b}$	$m_{\rm dm}$	$\epsilon_{\rm com}$	$\epsilon_{\rm prop}$	$z_{\rm end}$
	$(h^{-1}\,{\rm Mpc})$		$(h^{-1}\,{\rm M}_\odot)$	$(h^{-1}\,{\rm M}_\odot)$	$(h^{-1}\,{\rm kpc})$	$(h^{-1}\,{\rm kpc})$	
L006N128	6.25	128^3	1.4×10^6	6.3×10^6	1.95	0.5	2
L012N256	12.50	256^3	1.4×10^6	6.3×10^6	1.95	0.5	2
L025N128	25.00	128^3	8.7×10^7	4.1×10^8	7.81	2.0	0
L025N256	25.00	256^3	1.1×10^7	5.1×10^7	3.91	1.00	2
L025N512	25.00	512^3	1.4×10^6	6.3×10^6	1.95	0.5	1
L050N256	50.00	256^3	8.7×10^7	4.1×10^8	7.81	2.0	0
L050N512	50.00	512^3	1.1×10^7	5.1×10^7	3.91	1.0	0
L100N128	100.00	128^3	5.5×10^9	2.6×10^{10}	31.25	8.0	0
L100N256	100.00	256^3	6.9×10^8	3.2×10^9	15.62	4.0	0
L100N512	100.00	512^3	8.7×10^7	4.1×10^8	7.81	2.0	0

softening scales [1]. We use fixed comoving softening scales down to $z = 2.91$ below which we switch to a fixed proper scale. Our largest simulations use 2×512^3 particles in boxes of comoving size $L = 25$, 50, and $100\ h^{-1}\,{\rm Mpc}$.

The initial particle positions and velocities are obtained from glass-like (White 1994) initial conditions using CMBFAST (version 4.1; Seljak & Zaldarriaga 1996) and employing the Zeldovich approximation to linearly evolve the particles down to redshift $z = 127$. We assume a flat ΛCDM universe and employ the set of cosmological parameters $[\Omega_m, \Omega_b, \Omega_\Lambda, \sigma_8, n_s, h] = [0.238, 0.0418, 0.762, 0.74, 0.951, 0.73]$, as determined from the WMAP 3-year data and consistent[2] with the WMAP 5-year data (Komatsu et al. 2008). In addition, the primordial helium mass fraction was set to $X_{\rm H} = 0.248$.

We employ the star formation recipe of Schaye & Dalla Vecchia (2008), to which we refer the reader for details. Briefly, gas with densities exceeding the critical density for the onset of the thermo-gravitational instability ($n_{\rm H} \sim 10^{-2} - 10^{-1}\ {\rm cm}^{-3}$) is expected to be multiphase and star-forming (Schaye 2004). We therefore impose an effective equation of state with pressure $P \propto \rho_g^{\gamma_{\rm eff}}$ for densities exceeding $n_{\rm H} = 0.1\ {\rm cm}^{-3}$, normalized to $P/k = 10^3\ {\rm cm}^{-3}\,{\rm K}$ for an atomic gas at the threshold density. We use $\gamma_{\rm eff} = 4/3$ for which both the Jeans mass and the ratio of the Jeans length and the SPH kernel are independent of the density, thus preventing spurious fragmentation due to a lack of numerical resolution.

The local Kennicutt-Schmidt star formation law is analytically converted and implemented as a pressure law. As we demonstrated in Schaye & Dalla Vecchia (2008),

[1] We give the Plummer equivalent values, that is to say, that the Newtonian potential of a point mass in non-periodic space is Gm/ϵ, the same as for a Plummer 'sphere' of size ϵ (see Springel 2005, for more details)

[2] Our value of σ_8 is $1.6\,\sigma$ lower than allowed by the WMAP 5-year data.

our method allows us to reproduce arbitrary input star formation laws for any equation of state without tuning any parameters. We use the observed Kennicutt (1998) law,

$$\dot{\Sigma}_* = 1.5 \times 10^{-4}\,\mathrm{M_\odot yr^{-1} kpc^{-2}} \left(\frac{\Sigma_\mathrm{g}}{1\,\mathrm{M_\odot pc^{-2}}}\right)^{1.4}, \tag{3.1}$$

where we divided Kennicutt's normalization by a factor 1.65 to account for the fact that it assumes a Salpeter IMF whereas we are using a Chabrier (2003) IMF.

Galactic winds are implemented as described in Dalla Vecchia & Schaye (2008). Briefly, after a short delay of $t_\mathrm{SN} = 3 \times 10^7$ yr, corresponding to the maximum lifetime of stars that end their lives as core-collapse supernovae, newly-formed star particles inject kinetic energy into their surroundings by kicking a fraction of their neighbours in a random direction. The simulations presented here use the default parameters of Dalla Vecchia & Schaye (2008), which means that each SPH neighbour i of a newly-formed star particle j has a probability of $\eta m_j / \sum_{i=1}^{N_\mathrm{ngb}} m_i$ of receiving a kick with a velocity v_w. We choose $\eta = 2$ and $v_\mathrm{w} = 600\ \mathrm{km\,s^{-1}}$ (i.e., if all baryonic particles had equal mass, each newly formed star particle would kick, on average, two of its neighbours). Assuming that each star with initial mass in the range $6 - 100\ \mathrm{M_\odot}$ injects $10^{51}\ \mathrm{erg}$ of kinetic energy, these parameters imply that the total wind energy accounts for 40 per cent of the available kinetic energy for a Chabrier IMF and a stellar mass range $0.1 - 100\ \mathrm{M_\odot}$ (if we consider only stars in the mass range $8 - 100\ \mathrm{M_\odot}$ for type II SNe, this works out to be 60 per cent). The value $\eta = 2$ was chosen to roughly reproduce the peak in the cosmic star formation rate. Note that contrary to the widely-used kinetic feedback recipe of Springel & Hernquist (2003), the kinetic energy is injected *locally* and the wind particles are *not* decoupled hydrodynamically. As discussed by Dalla Vecchia & Schaye (2008), these differences have important consequences.

Radiative cooling was implemented according to chapter 2[3]. In brief, net radiative cooling rates are computed element-by-element in the presence of the cosmic microwave background (CMB) and a Haardt & Madau (2001, hereafter HM01) model for the UV/X-ray background radiation from quasars and galaxies. The contributions of the eleven elements hydrogen, helium, carbon, nitrogen, oxygen, neon, magnesium, silicon, sulphur, calcium, and iron are interpolated as a function of density, temperature, and redshift from tables that have been pre-computed using the publicly available photo-ionization package CLOUDY, last described by Ferland et al. (1998), assuming the gas to be optically thin and in (photo-)ionization equilibrium.

Hydrogen reionization is implemented by turning on the evolving, uniform ionizing background at redshift $z = 9$. Prior to this redshift the cooling rates are computed using the CMB and a photo-dissociating background which we obtain by cutting off the $z = 9$ HM01 spectrum at 1 Ryd. Note that the presence of a photo-dissociating background suppresses H_2 cooling at all redshifts.

Our assumption that the gas is optically thin may lead to an underestimate of the temperature of the IGM shortly after reionization (e.g. Abel & Haehnelt 1999). Moreover, it is well known that without extra heat input, hydrodynamical simulations underestimate the temperature of the IGM at $z \gtrsim 3$, the redshift around which helium

[3]We used their equation (3) rather than (4) and CLOUDY version 05.07 rather than 07.02.

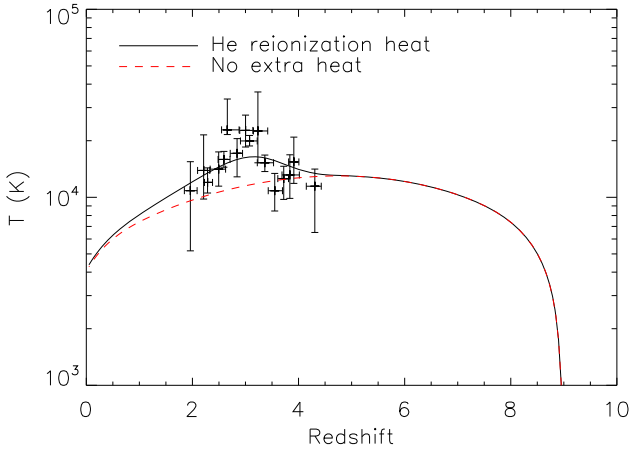

Figure 3.1: A comparison between the simulated and observed evolution of the temperature of gas with density equal to the cosmic mean. The dashed curve indicates the temperature evolution for a gas parcel undergoing Hubble expansion, computed using the same radiative cooling and heating rates as are used in our simulations for gas of primordial composition. These net cooling rates include the effects of the CMB and, below $z = 9$, of the evolving UV/X-ray background (UVB) from galaxies and quasars as modeled by HM01, assuming the gas to be optically thin and in ionization equilibrium. The redshift of hydrogen reionization was set to $z = 9$ by turning on the UVB at this redshift, resulting in a steep increase of the temperature to $T \sim 10^4$ K. A comparison with with the data points of Schaye et al. (2000), which were derived from the widths of Lyα absorption lines, shows that the simulation underestimates the temperature at $z \approx 3$, the redshift around which the reionization of helium is thought to have ended. To mimic the expected extra heat input, relative to the optically thin limit, during helium reionization, the solid curve shows the result of injecting an extra 2 eV per proton, smoothed with a $\sigma(z) = 0.5$ Gaussian centered at $z = 3.5$. The reduced χ^2 for the solid and dashed curves is 1.1 and 4.5, respectively.

reionization is thought to have ended (e.g. Theuns et al. 1998, 1999; Bryan et al. 1999; Schaye et al. 2000; Ricotti et al. 2000). We therefore inject $2\ \mathrm{eV}$ per proton, smoothed with a $\sigma(z) = 0.5$ Gaussian centered at $z = 3.5$. Figure 3.1 shows that with this extra energy, the predicted temperature at the mean density agrees well with the measurements of Schaye et al. (2000).

3.3 Ingredients from stellar evolution

Cosmological simulations cannot at present resolve individual stars. Instead, a single particle is taken to represent a population of stars of a single age, a so-called simple stellar population (SSP), with some assumed stellar initial mass function (IMF). The task of stellar evolution modules in cosmological hydrodynamical simulations is to implement the timed release of kinetic energy and mass by star particles. The feedback processes originating from stellar evolution that we will consider are winds from asymptotic giant branch (AGB) stars, type Ia supernovae (SNe), type II (i.e. core collapse) SNe[4] and the winds from their progenitors. The above stellar processes differ in a number of ways, such as their nucleosynthetic production, their energetic output, and the timescale on which they act.

Progenitors associated with AGB stars are typically intermediate mass ($0.8\ \mathrm{M}_\odot \leq M \leq 8\ \mathrm{M}_\odot$) stars which have long ($10^8\ \mathrm{yr} \lesssim \tau \lesssim 10^{10}\ \mathrm{yr}$) main sequence lifetimes (see Kippenhahn & Weigert 1994). For AGB stars the mass loss occurs during a period that is very short compared with both their lifetimes and the dynamical timescales in cosmological simulations and we therefore assume the mass loss for an AGB star of given mass to happen within a single simulation time step at the end of the main sequence lifetime. The kinetic energy injected by AGB stars is assumed to be unimportant, which is an excellent approximation both because observed AGB wind velocities are not large compared to the velocity dispersion in the ISM and because it takes an SSP billions of years for all the energy to be released. AGB stars are major producers of carbon and nitrogen, both of them being among the few elements that can be detected in the diffuse IGM (e.g. Schaye et al. 2003; Fechner & Richter 2008).

Since type II SNe (SNII) only result from massive stars (see Crowther & Smartt 2007, and references therein), most of these events take place within tens of millions of years after the birth of a stellar population. For SNII progenitors mass loss on the main sequence can be substantial. However, since their main sequence lifetimes are short compared with the dynamical timescales in cosmological simulations, it is still a good approximation to release all the mass ejected by stars of a fixed initial mass in a single time step at the end of their lifetimes. Note that if the time step governing a star particle is shorter than the lifetime of the least massive SNII progenitor, then the mass will still be ejected over multiple time steps.

Type II SNe explosions dump so much energy in the ISM ($\sim 10^{51}\ \mathrm{erg}$ of kinetic energy per SN) in a short time that they may drive galactic-scale outflows from starburst-

[4]Type Ib and Ic SN are also core collapse supernova, but we follow other authors and use type II to refer to the entire class of core collapse SN.

ing galaxies (e.g. Veilleux et al. 2005). The implementation of these winds is troublesome since simulations lack the resolution to implement them correctly (e.g. Ceverino & Klypin 2007; Dalla Vecchia & Schaye 2008). In our simulations forty percent of the kinetic energy from SNII is injected in kinetic form as discussed in section 3.2 and in more detail in Dalla Vecchia & Schaye (2008). The remainder is assumed to be lost radiatively on scales below the resolution limit of the simulation.

Unlike type II SNe and AGB stars, type Ia SNe are a result of binary stellar evolution, and consequently somewhat complicated to model. Currently there are two major theories for the progenitors of type Ia SNe. The most common is the single degenerate model. In this model, a white dwarf experiences enough mass transfer via a main sequence or giant companion to bring its mass above the Chandrasekhar limit, inducing an explosion. According to the double degenerate model, two white dwarfs merge after a long period of binary evolution. In order to predict the type Ia SN rate from a stellar population, one must consider a wide range of relatively uncertain processes (e.g. binary stellar evolution) and poorly constrained parameters (e.g. binary fraction, binary separation, binary mass function).

Although each SNIa is thought to inject a similar amount of kinetic energy as a type II SN, they are thought to be much less efficient at driving galactic outflows, mainly because the energy of a stellar population is released over billions of years rather than the tens of millions of years over which core collapse SNe release their energy. SNIa may, however, dominate the stellar energy feedback in galaxies with very low specific star formation rates. We therefore do include energy feedback by SNIa, which we distribute in thermal form among the SPH neighbours of star particles.

These two types of supernovae also have different chemical signatures. Type II SNe produce copious amounts of oxygen and so-called 'alpha elements' (neon, magnesium, silicon, etc.). These elements are primarily a result of α-capture reactions and, in addition to oxygen, make up the bulk of the metal mass ejected from type II SNe (Woosley & Weaver 1995). What is known about type Ia SNe (SNIa) is that they are a major source of iron in the Universe and that a large fraction of them involve relatively old ($\gtrsim 10^9$ yr) stars (see Greggio & Renzini 1983). Because of the time difference between the release of α elements by type II SNe and iron by SN Ia, the α/Fe ratio can provide information about the time since the last starburst, at least for the case of closed box models.

Before discussing our implementation of mass transfer from star particles, we briefly discuss all the ingredients of our stellar evolution module: the IMF, the stellar lifetimes, the type Ia SN rate and the stellar yields.

3.3.1 Stellar initial mass function

The stellar IMF has long been a subject of debate. Salpeter (1955) made the first attempt to derive an IMF from local stellar counts and his formulation is still widely used today. As star formation is still not understood well enough to predict the IMF from first principles, a wide range of IMFs are available in the literature (e.g., Romano et al. 2005). Although there is consensus about the fact that the IMF is less steep than

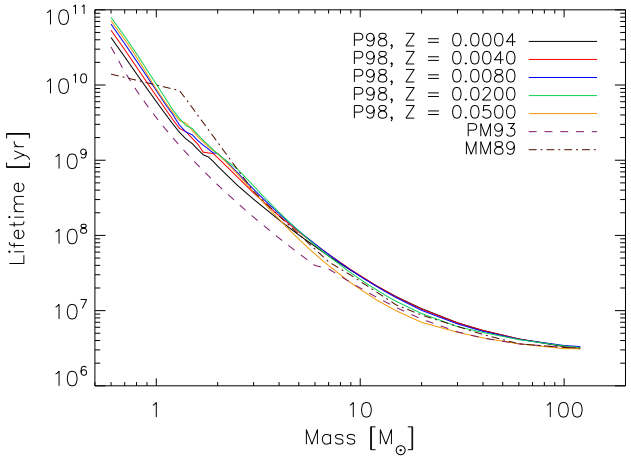

Figure 3.2: Stellar lifetime as a function of initial mass for various metallicities (metal mass fractions). Solid lines show lifetimes as given by Portinari et al. (1998), while the dot-dashed line shows calculations from Padovani & Matteucci (1993), who compiled results from the literature for a unspecified metallicity, and the dashed line shows the lifetimes given by Maeder & Meynet (1989a), who assumed solar abundances. Lifetime is a strongly decreasing function of mass, but it is only weakly dependent on metallicity.

Salpeter below $1\ \mathrm{M}_\odot$, there are many uncertainties. In addition, the IMF may depend on redshift or on properties of the environment such as metallicity, gas pressure, or the local radiation field.

For our purposes, the particularly interesting IMFs are the Salpeter IMF - because it serves as a reference model and because it is still used in many simulations - and the Chabrier (2003) IMF - because it is an example of an IMF with a low mass turnover that fits the observations much better than the Salpeter IMF. In this work we will assume a Chabrier IMF.

The Salpeter mass function takes a very simple power-law form,

$$\Phi(M) \equiv \frac{dN}{dM} = AM^{-2.35}, \tag{3.2}$$

where the normalization constant A is chosen such that:

$$\int M\Phi(M)dM = 1\ \mathrm{M}_\odot. \tag{3.3}$$

While the Chabrier IMF has the advantage that it does not overproduce low mass stars, it is slightly more complicated:

$$M\Phi(M) = \begin{cases} Ae^{-(\log M - \log M_\mathrm{c})^2/2\sigma^2} & \text{if } M \leq 1\mathrm{M}_\odot \\ BM^{-1.3} & \text{if } M > 1\mathrm{M}_\odot \end{cases} \tag{3.4}$$

where $M_\mathrm{c} = 0.079$, $\sigma = 0.69$, and the coefficients A and B are set by requiring continuity at $1\ \mathrm{M}_\odot$ and by the normalization condition (3.3). Although the shape of the IMF above $1\ \mathrm{M}_\odot$ is very similar to Salpeter, the lognormal decrease at the low mass end results in a much lower stellar mass-to-light ratio.

Besides the shape of the IMF, we also need to specify the mass limits. The lower limit is defined by the hydrogen burning limit of a star (typically cited as $0.08\ \mathrm{M}_\odot$; e.g.

Table 3.3: AGB yield references and grids

Ref.	Initial stellar mass ($M_\odot$)	Metallicity
HG97	[0.8, 0.9, 1, 1.3, 1.5, 1.7, 2, 2.5, 3, 3.5, 4, 4.5, 5, 6, 7, 8]	[0.001, 0.004, 0.008, 0.02, 0.04]
M01	(various) [0.85 - 5]	[0.004, 0.008, 0.019]
I04	[0.5, 1, 1.5, 2, 2.5, 3, 3.5, 4, 4.5, 5, 5.5, 6, 6.5, 7, 7.5, 8]	[0.0001, 0.004, 0.008, 0.02]

Kippenhahn & Weigert 1994), while the upper limit is significantly more uncertain, and the value most often found in the literature of $100\ M_\odot$ roughly reflects the current upper limit of observed stars. For consistency with previous studies, we choose mass limits of $0.1\ M_\odot$ and $100\ M_\odot$.

3.3.2 Stellar lifetimes

Although a star can be active (via accretion) for an indefinite period of time, it is useful to define its stellar 'lifetime' as the time a star takes to move from the zero age main sequence up the giant branch and through any subsequent giant evolution. Using this definition, most stellar mass loss occurs at the end of the star's lifetime during the AGB/SN phase.

There is no easy way to determine the lifetime function for a stellar population observationally. As a result, the published lifetimes are functional fits to the results of stellar evolution models (e.g., Maeder & Meynet 1989a and Padovani & Matteucci 1993; see Romano et al. 2005 for an overview).

Portinari et al. (1998) have published metallicity-dependent lifetimes from their stellar evolution calculations in tabular form and we show their results in figure 3.2 together with the widely used lifetimes of Maeder & Meynet (1989a), who assumed solar abundances, and Padovani & Matteucci (1993), who presented a compilation taken from the literature but did not specify the assumed metallicity. The different lifetime sets agree well at high mass, but differ by nearly an order of magnitude for stars of a few solar masses with Padovani & Matteucci (1993) giving systematically lower values.

Lifetime is a strongly decreasing function of mass and only weakly dependent on metallicity. Although metallicity seems to make little difference, it is attractive to be consistent in treating stellar evolution (in that we use yields based on the same calculations). We thus employ the metallicity-dependent lifetime tables of Portinari et al. (1998).

3.3.3 Stellar yields

The mass ejected in each element must be obtained from stellar evolution and (explosive) nucleosynthesis calculations. Differing treatments of physics can often lead to drastically different results in yield calculations. For instance, is it largely unknown what determines the convection boundaries and hot-bottom burning in AGB stars,

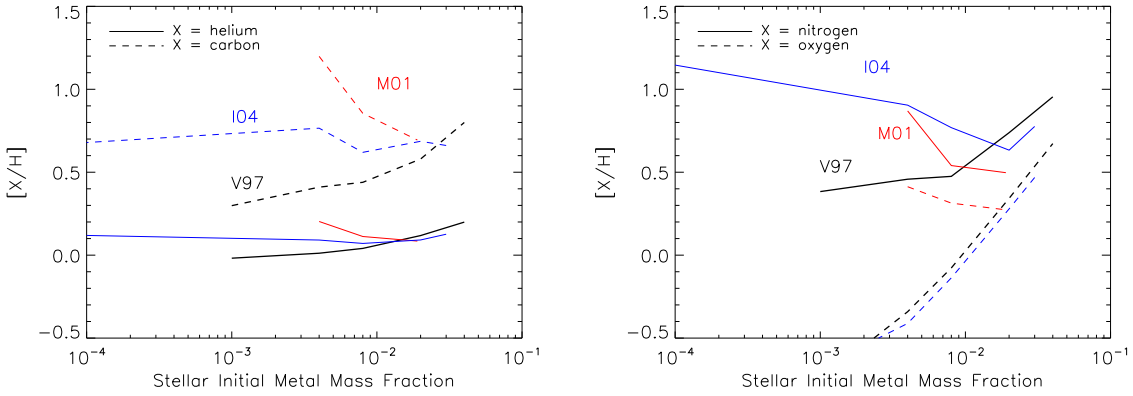

Figure 3.3: Composition of the integrated AGB ejecta of an SSP at time $t = \infty$ as a function of its initial stellar metal mass fraction, assuming the yields of van den Hoek & Groenewegen (1997) (black, thick lines), Marigo (2001) (red, medium thick lines), or Izzard et al. (2004) (blue, thin lines). Shown are the abundances of helium (*left, solid*), carbon (*left, dashed*), nitrogen (*right, solid*) and oxygen (*right, dashed*) relative to hydrogen in solar units. The calculations assume a Chabrier IMF and integrate the yields over the stellar initial mass range $[0.8, 6]$ $\mathrm{M}_\odot$. The different yield sets agree around solar metallicity, but differ significantly for lower metallicities.

leading to discrepancies between yields sets[5], as we will see below. Hirschi et al. (2005) found that adding rotation to type II SN models changes the yields by factors ranging from two to an order of magnitude. These problems are most evident in the fact that the yields of individual elements are often rescaled in order to get chemical evolution models to match observations. In fact, some authors (e.g. François et al. 2004) use observations and chemical evolution models to derive stellar yields for a number of elements, and the results show marked differences from yields derived from nucleosynthetic calculations.

Another important point to make sure of when using yields from various processes, is that the theoretical assumptions made in the models match. For instance, if one uses AGB yields for masses up to $8\ \mathrm{M}_\odot$, then one must take care to use type II SNe yields that begin higher than $8\ \mathrm{M}_\odot$ (Marigo 2001). The problem is more often than not in reverse, however, since most yield sets for massive stars are tabulated down to $\approx 10\ \mathrm{M}_\odot$, but most intermediate mass yield sets only go up to at most $8\ \mathrm{M}_\odot$, leaving it up to the user to decide what to do for the transition masses. Ideally, one would like to use a consistent set of yields, in the sense that the same stellar evolution model is used for both intermediate mass stars and the progenitors of core collapse SNe.

AGB stars

The asymptotic giant branch phase of stellar evolution occurs in intermediate mass stars near the very end of their lifetimes. During this phase the envelope of the star

[5]In this section we use the term yield in the generic sense, referring to stellar ejecta. We will define it more rigorously in section 3.5.1.

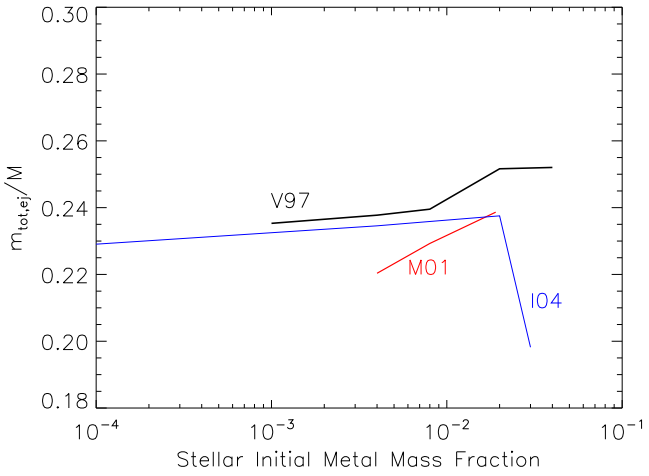

Figure 3.4: Total fraction of the initial mass of an SSP ejected by AGB stars at time $t = \infty$ as a function of initial stellar metal mass fraction, assuming the yields of van den Hoek & Groenewegen (1997) (black, thick lines), Marigo (2001) (red, medium thick lines), or Izzard et al. (2004) (blue, thin lines). The calculations assume a Chabrier IMF and integrate the yields over a stellar initial mass range $[0.8, 6]\ \mathrm{M}_\odot$, but the fractions are normalized to the mass range $[0.1, 100]\ \mathrm{M}_\odot$. Different yield sets predict similar ejected mass fractions. The ejected mass fraction is insensitive to metallicity.

puffs up and is eventually shed, causing the star to lose up to 60 % of its mass. Prior to the AGB phase, material in the core (where most of the heavy elements reside) is dredged up into the envelope via convection. As a result, the ejecta are particularly rich in carbon and nitrogen.

Building on pioneering work by Iben & Truran (1978) and Renzini & Voli (1981), various groups have published AGB yields (e.g. Forestini & Charbonnel 1997; van den Hoek & Groenewegen 1997; Marigo 2001; Chieffi et al. 2001; Karakas et al. 2002; Izzard et al. 2004). Table 3.3 outlines the extent of the resolution (in mass and metallicity) of the AGB yields of van den Hoek & Groenewegen (1997), Marigo (2001) and Izzard et al. (2004), which are some of the most complete sets for our purposes. These yields are compared in Fig. 3.3, which shows the abundance relative to hydrogen, in solar units[6], of various elements in the ejecta as a function of stellar metallicity. These calculations are for an SSP with a Chabrier IMF and the mass range $[0.8, 6]\ \mathrm{M}_\odot$ at time $t = \infty$. The yields agree very well at solar metallicity, and for the case of helium, this agreement extends to lower metallicities. However, for nitrogen, oxygen, and particularly carbon, different yields sets give very different results at low metallicities.

We show in Fig. 3.4, for each yield set, the integrated fraction of the initial SSP mass ejected by stars in the mass range $[0.8, 6]\ \mathrm{M}_\odot$ at time $t = \infty$, normalized to the total initial stellar mass over the range $[0.1, 100]\ \mathrm{M}_\odot$. The ejected mass fractions are very similar for the different yield sets.

In this work we use the yields of Marigo (2001). Although these only go up to $5\ \mathrm{M}_\odot$, they form a complete set with the SN Type II yields of Portinari et al. (1998) since they are both based on the Padova evolutionary tracks. Indeed, there are very few yield pairings that form a consistent set across the full mass range.

[6]We use the notation $[\mathrm{X/H}] \equiv \log(\mathrm{X/H}) - \log(\mathrm{X/H})_\odot$.

Table 3.4: SN type II yield references and grids

Ref.	Initial stellar mass ($M_\odot$)	Metallicity
WW95	[11, 12, 13, 15, 18, 19, 20, 22, 25, 30, 35, 40]	[0.0, 0.000002, 0.0002, 0.002, 0.02]
P98	[6, 7, 9, 12, 15, 20, 30, 60, 100, 120, 150, 200, 300, 500, 1000]	[0.0004, 0.004, 0.008, 0.02, 0.05]
CL04	[13, 15, 20, 25, 30, 35]	[0.0, 0.000001, 0.0001, 0.001, 0.006, 0.02]

Type II Supernovae

Although major advances have been made in modelling type II SNe, theorists have yet to come up with a model that self-consistently explodes. As a result, the yields are very sensitive to the location of the mass cut, i.e., the explosion radius. The material interior to this radius is assumed to end up in the stellar remnant, while the mass exterior to this radius is assumed to be ejected in the explosion. Unfortunately, the mass cut is very uncertain, thus creating another degree of freedom. Although uncertainties in the explosion radius do not affect the oxygen yields much, the yields of heavier elements such as iron are very sensitive to this choice.

A large number of groups have published tables of type II SN yields (e.g., Maeder 1992; Woosley & Weaver 1995; Portinari et al. 1998; Rauscher et al. 2002; Hirschi et al. 2005; Nomoto et al. 2006). Although the more recent models tend to be more sophisticated, for example including the effects of improved stellar and nuclear physics and rotation, the Woosley & Weaver (1995) yields are still the most widely used. Portinari et al. (1998) combine models of pre-SN stellar mass loss with the nucleosynthesis explosion calculations of Woosley & Weaver (1995), who ignored pre-SN mass loss. To do this they link the carbon-oxygen core mass predicted by their models with those of Woosley & Weaver (1995). They find low metallicity, massive stars to have very inefficient mass loss for these large core masses (for which there are no type II SN yields), they only consider mass loss by winds and assume the rest of the star collapses directly into a black hole.

Table 3.4 and Figure 3.5 compare the SN type II yields of Woosley & Weaver (1995), Portinari et al. (1998), and Chieffi & Limongi (2004). Figure 3.5 shows the abundance relative to hydrogen, in solar units, of various elements in the ejecta as a function of stellar metallicity. The elements shown are those that, together with hydrogen, dominate the radiative cooling of (photo-)ionized plasmas chapter 2. These calculations are for an SSP with a Chabrier IMF in the mass range $[8, 40]$ $M_\odot$ at time $t = \infty$. It is clear that the yields of elements that are produced by type II SNe depend only weakly on metallicity, unless the metallicity is supersolar. However, except for very low metallicities, the nitrogen abundance in the ejecta is proportional to the stellar metallicity, indicating that it is simply passing through rather than being produced.

The different yield sets agree well for helium, carbon, and nitrogen, but there are large differences for heavier elements. The difference between Portinari et al. (1998) and Woosley & Weaver (1995) is due to the fact that the former add their stellar evolution to the Woosley & Weaver (1995) nucleosynthesis calculations. The difference between Chieffi & Limongi (2004) and Woosley & Weaver (1995) is caused mostly by

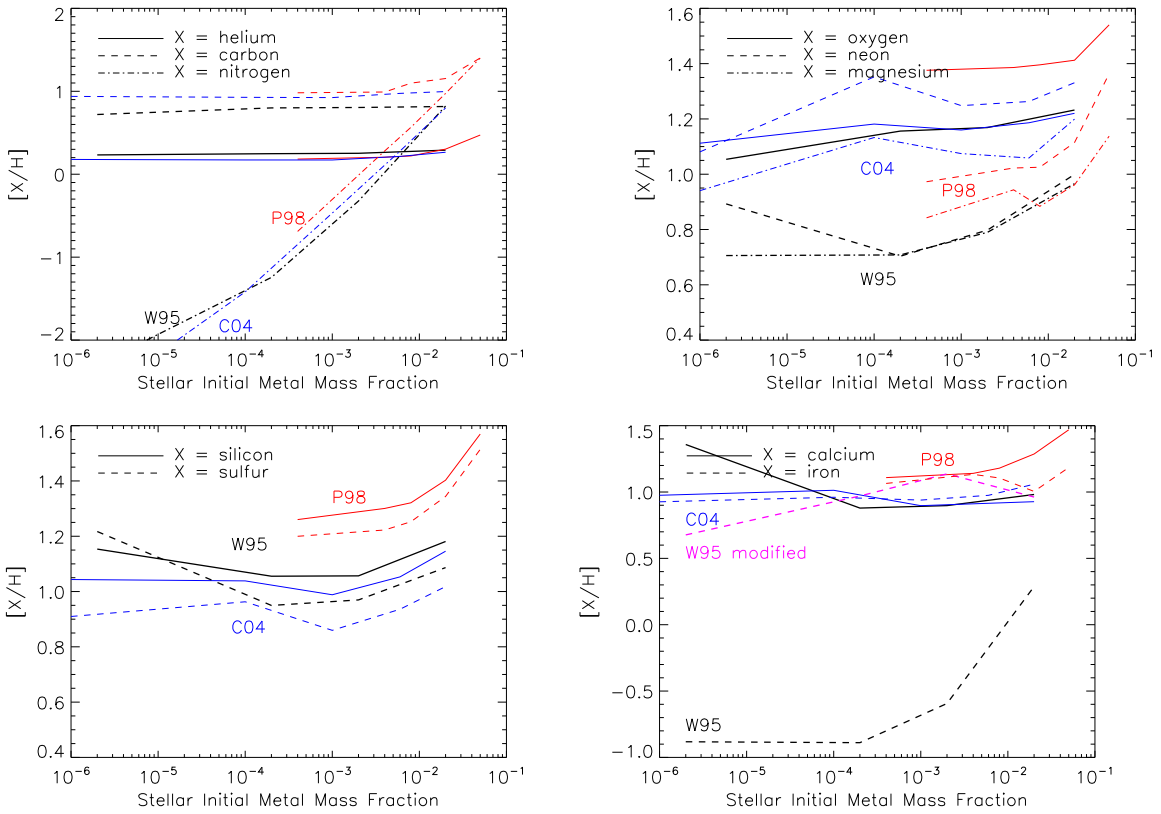

Figure 3.5: Composition of the integrated SN type II ejecta of an SSP at time $t = \infty$ as a function of its initial stellar metal mass fraction, assuming the yields of Woosley & Weaver (1995) (black, thick lines), Portinari et al. (1998) (red, medium thick lines), or Chieffi & Limongi (2004) (blue, thin lines). Shown are the abundances of helium, carbon, nitrogen, oxygen, neon, magnesium, silicon, sulphur, calcium, and iron, as indicated in the legends. The calculations assume a Chabrier IMF and integrate the yields over the stellar initial mass range $[8, 40]$ $M_\odot$. The black thick dashed line in the lower right panel indicates the result of transferring the ^{56}Ni to the Iron yield of Woosley & Weaver (1995). While the different yield sets agree well for the lightest elements (upper panels), there are large differences for elements heavier than nitrogen.

the difference in the assumed mass cut.

The yields presented in Woosley & Weaver (1995) consider the state of the ejecta 10^5 s after the explosion. Because a number of isotopes have rather short decay times, it is customary to consider – as most recent yield sets have done – the state of the ejecta at a much later time (10^8 s in the case of Chieffi & Limongi 2004). This is especially important for ^{56}Ni, which decays rapidly into ^{56}Fe. When Portinari et al. (1998) incorporate the Woosley & Weaver (1995) yields into their calculations, they simply add the ^{56}Ni to the ^{56}Fe. We have added an additional magenta line to figure 3.5 to show the iron yield from Woosley & Weaver (1995) with this adjustment. This agrees much better with the other two yield sets.

Figure 3.6 shows the integrated fraction of the initial mass of an SSP that is ejected by type II SNe at time $t = \infty$ as a function of metallicity. These calculations again

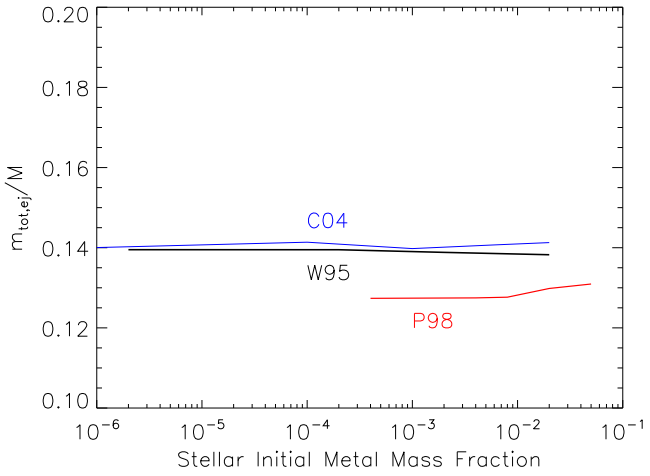

Figure 3.6: Total fraction of the initial mass of an SSP ejected by SNe type II at time $t = \infty$ as a function of initial stellar metal mass fraction, assuming the yields of Woosley & Weaver (1995) (black, thick lines), Portinari et al. (1998) (red, medium thick lines), or Chieffi & Limongi (2004) (blue, thin lines). The calculations assume a Chabrier IMF and integrate the yields over the stellar initial mass range $[8, 40]$ $\mathrm{M}_{\odot}$, but the fractions are normalized tot he mass range $[0.1, 100]$ $\mathrm{M}_{\odot}$. The ejected mass fraction is insensitive to metallicity and different yields sets predict very similar results.

assume a Chabrier IMF and integrate the yields over the mass range $[8, 40]$ $\mathrm{M}_{\odot}$, but normalize the mass fraction to the mass range $[0.1, 100]$ $\mathrm{M}_{\odot}$. The ejected mass is insensitive to metallicity and the three yield sets are in excellent agreement.

We use the yields of Portinari et al. (1998) since they include mass loss from massive stars and because they form a self-consistent set together with the stellar lifetimes of these authors and the AGB yields of Marigo (2001). Their models allow for the possibility of electron capture supernova for intermediate mass stars ($7-9$ $\mathrm{M}_{\odot}$). Unfortunately, nucleosynthesis calculations for these stars have only recently been performed (e.g., Wanajo et al. 2008). The Portinari et al. (1998) yields therefore only consider the shedding of the envelope and the mass loss up to that stage. While both Chieffi & Limongi (2004) and Woosley & Weaver (1995) evolve their models until the point of supernova and then begin supernova calculations, they do not include mass loss in their yield tables (since the goal of their studies was to investigate explosive nucleosynthesis).

Following the recommendation of L. Portinari (private communication), we have adjusted the massive star yields by the factors inferred from comparisons of chemodynamical models and current Galactic abundances. Following Portinari et al. (1998), we have multiplied the type II SN yields of C, Mg, and Fe for all masses and metallicities by factors of 0.5, 2, and 0.5, respectively. Note that these factors were *not* included in Fig. 3.5, but have been implemented for the rest of this work. The adjustments to Mg and Fe can be justified due to uncertainties in the explosive nucleosynthesis models by Woosley & Weaver (1995) as discussed by a number of authors (e.g. Timmes et al. 1995; Lindner et al. 1999; Carigi 2000; Goswami & Prantzos 2000; Carigi 2003; Gavilán et al. 2005; Nykytyuk & Mishenina 2006). These adjustments have also been incorporated into other studies (e.g. Liang et al. 2001; Lia et al. 2002; Portinari et al. 2004; Nagashima et al. 2005). These *ad hoc* adjustments reveal just how uncertain the yields are.

Type Ia Supernovae

Despite the fact that the progenitors of type Ia SNe are still uncertain, yield calculations can be made based on an explosion of a Chandrasekhar mass carbon-oxygen dwarf. While most models assume the progenitor to be a binary system, the yields usually consider just the explosion of the white dwarf itself, ignoring the companion completely.

It is instructive to anticipate a few features of these calculations. First, since a type Ia SN explosion occurs as soon as the compact object reaches the Chandrasekhar mass, the yields from this process will be independent of the initial stellar mass. Second, by the time a star gets to the white dwarf phase, it is almost completely composed of carbon, nitrogen and oxygen, and while the balance between these elements may depend on initial mass or composition, the models assume such a dependence is insignificant.

Several research groups have published yields from type Ia SNe. Their calculations range from one- to three-dimensional calculations (Travaglio et al. 2004). The standard to which most results are compared is the spherically symmetric calculation dubbed "W7" (Nomoto et al. 1984, 1997; Iwamoto et al. 1999; Brachwitz et al. 2000; Thielemann et al. 2003). We use the latest incarnation (at the time of code development) of the W7 model, i.e., Thielemann et al. (2003).

3.3.4 SN type Ia rates

The recipes for the release of mass by AGB stars and SNII are quite simple because these processes are direct results of stars reaching the ends of their lifetimes. Hence, one merely needs to combine the IMF with the stellar lifetime function and the yields and integrate over the time interval specified. The recipe for SNIa is, however, somewhat more complex.

Two SNIa channels are thought to be most plausible (see, e.g., Podsiadlowski et al. 2008 for a review). According to the single degenerate scenario, SNIa result when accretion onto a white dwarf by a binary companion pushes the former over the Chandrasekhar mass. The double degenerate scenario, on the other hand, involves the merger of two white dwarfs, thus putting the merger product over the Chandrasekhar mass.

The SNIa rate of an SSP as a function of its age can be determined using late age stellar and binary evolution theory. The formulation that is used most often is given by Greggio & Renzini (1983). This formulation requires knowledge of the distribution of secondary masses in binaries and makes some assumptions about binary evolution. These are poorly constrained and may therefore be subject to large uncertainties. Hence, it is attractive to take an alternative, more empirical approach. Guided by observations of SNIa rates, we can simplify the prescription by specifying a functional form for the empirical delay time function $\xi(t)$, which gives the SNIa rate as a function of the age of an SSP, normalized such that $\int_0^\infty \xi(t)dt = 1$. The parameters of this function can then be determined by fitting to observations of SNIa rates (e.g., Barris & Tonry 2006; Förster et al. 2006).

The number of SNIa explosions per unit stellar mass in a time step Δt for a given SSP is then

$$N_{\rm SNIa}(t; t+\Delta t) = \nu \int_{t}^{t+\Delta t} \xi(t')dt', \tag{3.5}$$

where ν is the number of SNe per unit formed stellar mass that will ever occur. While this approach is attractive since it does not require us to make any assumptions regarding the progenitors, we will employ yields that correspond to a scenario involving at least one white dwarf so the SNIa rate should take that into account (i.e., we should not have any SNIa before the white dwarfs have evolved). We therefore take an approach similar to Mannucci et al. (2006) and write:

$$N_{\rm SNIa}(t; t+\Delta t) = a \int_{t}^{t+\Delta t} f_{\rm wd}(t')\xi(t')dt', \tag{3.6}$$

where a is a normalization parameter and $f_{\rm wd}(t)$ is the number of stars that have evolved into white dwarfs up until time t (i.e., the age of the SSP) per unit initial stellar mass:

$$f_{\rm wd}(t) = \begin{cases} 0 & \text{if } M_Z(t) > m_{\rm wdhigh} \\ \displaystyle\int_{m_{\rm SNIalow}(t)}^{m_{\rm wdhigh}} \Phi(M)dM & \text{otherwise} \end{cases} \tag{3.7}$$

Here $m_{\rm wdhigh}$ and $m_{\rm wdlow}$ are the maximum and minimum white dwarf masses respectively, $M_Z(\tau)$ is the inverse[7] of the lifetime function $\tau_Z(M)$, and

$$m_{\rm SNIalow}(t) = \max(M_Z(t), m_{\rm wdlow}). \tag{3.8}$$

Note that the shape of the SNIa rate as a function of time differs between equations (3.5) and (3.6).

It is thought that stars with main sequence masses between $3\ {\rm M}_\odot$ and $8\ {\rm M}_\odot$ evolve into a SNIa progenitor white dwarf. Note that while our type II SN yields range to masses as low as $6\ {\rm M}_\odot$, the models used in the yield calculations of Portinari et al. (1998) for stars of 6 and $7\ {\rm M}_\odot$ do not incorporate any explosive nucleosynthesis. They note that stars of these masses could explode as electron capture SNe *or* evolve to a thermally-pulsing AGB phase, thus simply shedding their envelopes.

The form of the delay function ξ has generated particular interest recently (e.g., Dahlen et al. 2004). The two types of delay functions that are most often considered, the so-called e-folding delay and Gaussian delay functions, are shown in figure 3.7. The e-folding delay function takes the form:

$$\xi(t) = \frac{e^{-t/\tau_{\rm Ia}}}{\tau_{\rm Ia}} \tag{3.9}$$

where $\tau_{\rm Ia}$ is the characteristic delay time. This delay approximates predictions made for the single degenerate scenario via population synthesis models.

[7]The lifetime function is invertible because it is a monotonic function of mass for a fixed metallicity.

The Gaussian delay function was motivated by high redshift observations by Dahlen et al. (2004), which show a marked decline in the SNIa rate beyond $z = 1$. It takes the form:

$$\xi(t) = \frac{1}{\sqrt{2\pi\sigma^2}} e^{-\frac{(t-\tau_{\rm Ia})^2}{2\sigma^2}} \tag{3.10}$$

where $\sigma = 0.2\tau_{\rm Ia}$ for 'narrow' distributions and $\sigma = 0.5\tau_{\rm Ia}$ for 'wide' distributions. Note that the integral of this particular function ($\int_0^\infty \xi(t)dt$ is only normalised to unity for $\sigma \ll \tau_{\rm Ia}$. Gaussian delay functions often feature long characteristic times ($\tau_{\rm Ia} = 4$ Gyr) in order to fit the data. Strengths and weaknesses exist for both delay functions, and are discussed in the references cited above. Unfortunately, the choice of distribution (including all the ensuing parameters) is rather poorly constrained. In particular, both the cosmic star formation rate and the type Ia rate contain large uncertainties beyond a redshift of 1. For instance, the type Ia rate quoted at $z = 1.6$ by Dahlen et al. (2004) is based on only two detection events.

In addition to the cosmic SNIa rate, Mannucci et al. (2006) attempt to use other observations to constrain the shape of the delay function. They cite the dependence of the SNIa rate on galaxy colour observed in the local universe (Mannucci et al. 2005) as well as a dependence on radio loudness observed by Della Valle et al. (2005). Their analysis suggests that the delay time function could have two components, a "prompt" mode and a "tardy" mode (see also Scannapieco & Bildsten 2005a). These modes may have physical counterparts with the two progenitor channels, but this is still uncertain. Using such a delay function could improve our fits to the observations marginally, but would introduce another unknown parameter (the ratio of contributions of the modes). Moreover, the e-folding delay function also includes significant prompt and late contributions. We therefore chose to use an e-folding delay function with $\tau_{\rm Ia} = 2$ Gyr, but have also performed one simulation with a Gaussian delay function using $\tau_{\rm Ia} = 3.3$ Gyr and $\sigma = 0.66$ Gyr. These parameter values were chosen to roughly agree with the constraints mentioned above. The coefficient a appearing in equation (3.6) was chosen to roughly match observations of the cosmic SNIa rate.

We plot the current measurements of the cosmic SNIa rate in figure 3.7. We have self-consistently adjusted all data points to our cosmology of choice[8], $(h, \Omega_m, \Omega_\Lambda) = (0.73, 0.238, 0.762)$. Note that the different SNIa measurements are strongly discrepant, indicating that the statistical errors have been underestimated and/or that some rates suffer from systematic errors.

The solid, black curve in Figure 3.7 shows the evolution of the SNIa rate in our L100N512 simulation, which used the e-folding time delay function and $a = 0.01$. Also shown (dashed, black curve) is the predicted type Ia rate for another simulation that is identical to L100N512 except for the fact that it uses the Gaussian delay function and $a = 0.0069$. The e-folding and Gaussian models result in reduced χ^2 values of 2.6 and

[8]Correcting for cosmology is important since observations are taken over a volume in co-moving space. For instance, the highest redshift point of Poznanski et al. (2007) is greater than that of Dahlen et al. (2004) when using their cosmology, but when converting to our cosmology the Dahlen et al. (2004) point is reduced by a greater amount since it was taken over a larger redshift range. Thus, our plot shows the Dahlen et al. (2004) point to be greater than the Poznanski et al. (2007) point.

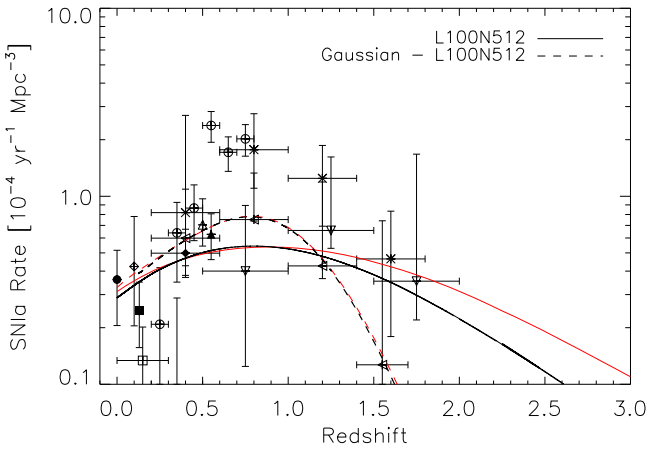

Figure 3.7: Volumetric Type Ia supernova rate as a function of redshift from our simulations (black) using either an e-folding (*solid*) or a Gaussian (*dashed*) delay function. Also shown are approximate fits using a "standard formulation" of the cosmic SNIa rate, calculated using equation (3.5) and the star formation history predicted by the simulations and a Chabrier IMF (red). The data points correspond to observations reported by Cappellaro et al. (1999) (filled circle), Madgwick et al. (2003) (open square), Blanc (2004) (filled square), Hardin (2000) (open diamond), Neill (2006) (filled diamond), Tonry (2003) (open black triangle), Pain (2002) (filled triangle), Dahlen et al. (2004) (crosses), Barris & Tonry (2006) (open circles), Poznanski et al. (2007) (upright triangles), and Kuznetsova et al. (2008) (left pointing triangles).

2.2, respectively. We consider this acceptable since the data are internally inconsistent. Note that the predicted SNIa rates agree better with the more recent measurements.

While preparing this publication, we encountered a bug in the code that resulted in $m_{\rm wdlow}$ being set to zero in equation (3.8). The net result is a shift in the effective delay time to lower redshifts and an increase in the effective value of a. Because this error complicates the interpretation of our parameter values and because most of the literature uses equation (3.5) rather than (3.6) we have tried to approximately match the SNIa rates predicted by our L100N512 simulations using equation (3.5), taking the star formation history predicted by the simulations as input and using the same (Chabrier) IMF as was used in the simulation. We expect the effects of this bug to be nominal, causing an increase in iron production at late times - increasing cooling slightly and releasing more metals from old stellar populations - but note that our rates still pass comfortably though the observations. Moreover, a simulation with a Gaussian delay function (which we will present in a later publication) showed negligible difference to the e-folding model in nearly all respects (e.g., star formation history, distribution of metals). The difference between the type Ia rates is much greater than the difference between the bugged and unbugged versions.

The matching "standard formulation" SNIa rates are shown as the red curves in

figure 3.7. The e-folding delay function (solid, red curve) uses $\tau_{\rm Ia} = 3$ Gyr while the Gaussian delay function (dashed, red curve) uses $\tau_{\rm Ia} = 3.3\ {\rm Gyr}, \sigma = 0.66\ {\rm Gyr}$ (which is identical to the original delay function used in combination with equation 3.6). When using equation (3.5) it is useful to parametrize the normalization in terms of η, the fraction of white dwarfs that eventually explode as SNIa, or the *Type Ia efficiency*, which is related to ν, the number of SNIa per unit formed stellar mass via

$$\eta \int_3^8 \Phi(M) dM = \nu \int_{0.1}^{100} M\Phi(M) dM. \tag{3.11}$$

The red curves in figure 3.7 correspond to $\eta = 2.50\ \%$ for the e-folding model and $\eta = 2.56\ \%$ for the Gaussian model. Note that these efficiencies correspond to our Chabrier IMF, whereas much of the literature quotes efficiencies for a Salpeter IMF. For a Salpeter IMF, these efficiencies work out to $\eta = 3.25\ \%$ and $\eta = 3.33\ \%$ for the e-folding model and the Gaussian model respectively.

We end the discussion by noting that we match another constraint in that we find iron abundances in our galaxies to be roughly solar at $z = 0$ (McCarthy et al. 2009).

3.4 Previous Work

Several authors have used similar chemodynamical models in previous studies. While these simulations are useful to compare to, it is important to pay close attention to the various parameters in each work. The earliest treatment that could truly be deemed chemodynamics was by Theis et al. (1992). While most of the subsequent codes (including ours) used SPH, they used a mesh code, and they explicitly tracked the evolution of metals as produced from stars, and even considered their impact on cooling.

Table 3.5 outlines the differences between a selection of previous simulations. It is important to note that some of these simulations were only run for individual galaxies while others used a large cosmological box. Note that in this table we only refer to the first paper in a series, but that the parameters shown are from the most recent incarnation of the model. We also include the type of model used for winds driven by supernovae.

It is useful to notice the trends that exist among the various authors. For the initial mass function Salpeter (1955) is regularly used as well as Arimoto & Yoshii (1987) (Kobayashi 2004b uses a simple power law of 1.10). Lia et al. (2002) published a formulation of the type Ia supernova rate given by Greggio & Renzini (1983), and many authors use this because it is concise and easy to follow. Others, however, follow very different recipes, such as Scannapieco et al. (2005) who use a type Ia supernova rate that is constant in time. The choice of a particular set of stellar lifetimes could have a strong effect on simulations since all of the feedback processes directly depend on it. Fortunately, the differences between the lifetimes are modest (see Romano et al. 2005 for a good review).

The treatment of cooling also has a significant impact on the outcome of the simulation. While cooling tables from Sutherland & Dopita (1993) are widely used, some

authors (Kawata & Gibson 2003; Kobayashi 2004b) have made their own cooling tables using the software package MAPPINGS III (Sutherland & Dopita (1993) used MAPPINGS II, and wrote both packages). None of the calculations published to date allow the relative contributions of the elements to vary, nor do they consider the effect of UV background on the metals.

Winds also play an important role. Some authors choose to inject gas surrounding a supernova event with thermal energy (often suppressing the cooling for sometime in order to ensure the feedback is effective) while others impart kinetic energy to the gas. Navarro & White (1993) proposed a hybrid method in which some fraction of the energy is given thermally and the remaining energy given kinetically.

Our simulations are similar in some respects to the previous works (i.e., stellar yields and lifetimes) but also have some new aspects such the way in which radiative cooling is implemented.

Table 3.5: Parameters of Previous Chemodynamical Simulations

Type	Year	Paper[a]	Code	IMF	SN Ia Rates	Lifetimes	Yields (SNII, Ia, AGB)	Cooling	Wind model
Galaxy	1992	TBH92[1]	TBH92[1]	S55[2]	immediate at death	MM89[3]	constant Z fractions	analytic	thermal
Galaxy	1995	SM95[4]	SM95[4]	MS79[5]	n/a	n/a	M87[6], n/a, n/a	n/a	thermal
Galaxy	1996	RVN96[7]	NW93[8]	KTG93[9]	GR83[10]	A93[11]	WW95[12], TNH93[13], n/a	n/a	NW93[8]
Galaxy	1999	B99[14]	CD-SPH	KTG93[9]	GR83[10]	RVN96[7]	WW95[12], NTY84[15], vdHG97[16]	DM72[17]	thermal
Galaxy	2001	K01[18]	K99[19]	S55[2]	T95[20]	constant	n/a	TBH92[1]	NW93[8]
Galaxy	2001	RME01[21]	RME01[21]	S55[2]	BMD98[22]	PM93[23]	WW95[12], NTY84[15], RV81[24]	n/a	kinetic
Cosmological	2001	M01[25]	APHMSPH	S55[2]	GR83[10]	immediate at death	WW95[12]/PCB98[26], TNH93[13], n/a	n/a	none
Galaxy	2002	LPC02[27]	LPC02[27]	S55[2]/AY87[28]	LPC02[27]	PCB98[26]	PCB98[26], I99[29], M01[30]	n/a	thermal
Galaxy	2003	KG03[31]	GCD+	S55[2] M = {0.2-60}	HKN99[32]	K97[33]	WW95[12], I99[29], vdHG97[16]	mpIII[34]	NW93[8]
Cluster	2003	V03[35]	n/a	various	LPC02[27]	n/a	WW95[12], I99[29], n/a	SD93[36]	thermal
Galaxy	2004	K04[37]	GRAPE-SPH	M^{α}, $\alpha = 1.10$	KTN00[38]	DFJ90[39]	N97[40], N97[41]	mpIII[34]	NW93[8]
Cluster	2004	T04[42]	GADGET-2	S55[2]/AY87[28]	M01[43]	PM93[23]	WW95[12], NIK97[44], RV81[24]	SD93[36]	kinetic
Cosmological	2005	C05[45]	GADGET-2	S55[2]	constant	constant	WW95[8], TNH93[9], n/a	SD93[36]	C05[45]
Galaxy	2006	MU06[46]	n/a	S55[2]	n/a	n/a	T95[20]	SD93[36]	thermal
Cluster	2006	R06[47]	FLY	S55[2]/AY87[28]	LPC02[27]	PCB98[26]	PCB98[26], I99[29], M01[30]	SD93[36]	thermal
Galaxy/Cosmological	2006	S06[48]	GASOLINE	MS79[5]	GR83[10]	A93[11]	WW95[12], TNH93[13], n/a	SD93[36]	thermal
Cosmological	2006	OD06[49]	GADGET-2	C03[50]	SB05[51]	BC03[52]	CL04[53], T95[20], M01[30]	SD93[36]	kinetic
Galaxy/Cosmological	2007	KSW07[54]	GADGET-2	S55[2]	KTN00[38]	DFJ90[39]	N97[40], N97[41]	mpIII[34]	thermal
					This Work				
Cosmological	2008	W09b[55]	GADGET-3	C03[50]	W09b[55]	PCB98[26]	PCB98[26], T03[56], M01[30]	W09a[57]	kinetic

[a] Here we cite only the first paper of the project, [1] Theis et al. (1992) (Eulerean code), [2] Salpeter (1955), [3] Maeder & Meynet (1989b), [4] Steinmetz & Muller (1995) ,[5] Miller & Scalo (1979), [6] Maeder (1987) , [7] Raiteri et al. (1996) , [8] Navarro & White (1993) , [9] Kroupa et al. (1993) , [10] Greggio & Renzini (1983) , [11] Alongi et al. (1993), [12] Woosley & Weaver (1995) , [13] Thielemann et al. (1993) , [14] Berczik (1999), [15] Nomoto et al. (1984), [16] van den Hoek & Groenewegen (1997), [17] Dalgarno & McCray (1972), [18] Kawata (2001) , [19] Kawata (1999), [20] Tsujimoto et al. (1995), [21] Recchi et al. (2001) (2 dimensional) , [22] Bradamante et al. (1998), [23] Padovani & Matteucci (1993), [24] Renzini & Voli (1981) , [25] Mosconi et al. (2001), [26] Portinari et al. (1998) , [27] Lia et al. (2002) , [28] Arimoto & Yoshii (1987) , [29] Iwamoto et al. (1999) , [30] Marigo (2001) , [31] Kawata & Gibson (2003) , [32] Hachisu et al. (1999) , [33] Kodama (1997) , [34] Tables made with Mappings III software, [35] Valdarnini (2003), [36] Sutherland & Dopita (1993), [37] Kobayashi (2004b), [38] Kobayashi et al. (2000), [39]David et al. (1990), [40] Nomoto et al. (1997), [41] Nomoto et al. (1997), [42] Tornatore et al. (2004), [43] Matteucci (2001) [44] Nomoto et al. (1997),[45] Scannapieco et al. (2005), [46] Mori & Umemura (2006), [47] Romeo et al. (2006), [48] Stinson et al. (2006), [49] Oppenheimer & Davé (2006), [50] Chabrier (2003), [51] Scannapieco & Bildsten (2005b), [52] Bruzual & Charlot (2003), [53] Chieffi & Limongi (2004), [54] Kobayashi et al. (2007), [55] Chapter 3, [56] Thielemann et al. (2003), [57] Chapter 2

3.5 THE MASS EJECTED BY A SIMPLE STELLAR POPULATION

The mass that is ejected during a single time step $(t, t + \Delta t)$ by a star particle of initial mass $m_{*,0}$ and metallicity Z that was created at time $t_* < t$ is given by

$$\Delta m_* = m_*(t) - m_*(t + \Delta t) \tag{3.12}$$

$$= m_{*,0} \int_{M_Z(t-t_*+\Delta t)}^{M_Z(t-t_*)} \Phi(M) m_{\rm ej}(M, Z)\, dM, \tag{3.13}$$

where $M_Z(\tau)$ is the inverse of the lifetime function $\tau_Z(M)$, $m_{\rm ej}(M, Z)$ is the mass ejected by a single star and $\Phi(M)$ is the IMF, normalized such that $\int M\Phi(M)dM = 1$. It is straightforward to generalize the above equations to give $\Delta m_{*,j}$, the mass ejected in the form of element j. The functions $\tau_Z(M)$ and $m_{j,\rm ej}(M, Z)$ need to be taken from stellar evolution and nucleosynthesis calculations provided in the literature.

3.5.1 Implementation

Since stellar evolution and nucleosynthesis depend on initial composition, a correct treatment of chemodynamics would require yields (i.e. the ejected mass of various elements) to be tabulated in a space with dimensionality equal to the number of elements. Most yields are, however, given only as a function of metallicity, where metallicity is the total mass fraction in metals. The models used to compute the yields assume implicitly that the relative abundances of the heavy elements are initially solar.

One way to implement the release of elements is to interpolate the ejected masses, which are given as a function of metallicity, to the metallicity of the star particle and to ignore possible differences between the relative abundances assumed by the yield calculation and the actual relative abundances of the star particle. However, this can have some very undesirable consequences. For example, because iron does not participate in the nucleosynthesis of intermediate mass stars, the iron that these stars eject was already present when the star was born. If an intermediate mass star has a high iron abundance for its metallicity, then simple interpolation of the yield tables with respect to metallicity would lead to a large underestimate of the ejected iron mass. That is, it would result in the spurious destruction of iron.

A more accurate way to implement chemodynamics would thus be to distinguish metals that were produced/destroyed from those that pass through the star without participating in the nucleosynthesis. If we knew, for each ejected element, what fraction of the ejected mass resulted from net nucleosynthetic production (i.e., production minus destruction) and what fraction simply passed through the star (the two fractions should add up to one), then it would make sense to assume that the mass that passed through the star is proportional to the star's initial abundance. In that case we would still neglect the effect of relative abundances on the nucleosynthesis itself (this can only be done by repeating the nucleosynthesis calculations or using the somewhat cumbersome Q-matrix formalism, e.g. Portinari et al. 1998), but we would take into account

the consequences of varying relative abundances on metals that do not participate in the nucleosynthesis.

We have adopted this strategy - as is often done (e.g. Recchi et al. 2001; Lia et al. 2002; Sommer-Larsen et al. 2005; Romeo et al. 2006; Tornatore et al. 2007) - and have implemented it as follows[9]. For a star of given initial mass and metallicity, we can write the mass of element j that is ejected into the surrounding medium, $m_{j,\mathrm{ej}}$, as the sum of two parts:

$$m_{j,\mathrm{ej}} = m_{j,0:\mathrm{ej}} + m_{j,\mathrm{p:ej}}. \tag{3.14}$$

Here $m_{j,0:\mathrm{ej}}$ is the mass in element j that would have been ejected if no nucleosynthesis had taken place and if the star were well-mixed,

$$m_{j,0:\mathrm{ej}} = \left(\frac{m_{j,0:\mathrm{star}}}{m_{\mathrm{tot},0:\mathrm{star}}}\right)_{\mathrm{sim}} \left(m_{\mathrm{tot,ej}}\right)_{\mathrm{tbl}}, \tag{3.15}$$

where $\left(m_{j,0:\mathrm{star}}/m_{\mathrm{tot},0:\mathrm{star}}\right)_{\mathrm{sim}}$ is the initial mass fraction of element j in the star *as tracked by the simulation* and $\left(m_{\mathrm{tot,ej}}\right)_{\mathrm{tbl}}$ is the total ejected mass according to the yield table. Note that we use the subscript "sim" to indicate values predicted by the simulation and the subscript "tbl" to indicate values that are published by authors presenting a particular set of stellar yields. The second term of equation (3.14) represents the ejected mass in element j that was produced minus destroyed. Assuming that the star is well-mixed, we can write it as

$$m_{j,\mathrm{p:ej}} = \left(m_{j,\mathrm{ej}}\right)_{\mathrm{tbl}} - \left(\frac{m_{j,0:\mathrm{star}}}{m_{\mathrm{tot},0:\mathrm{star}}}\right)_{\mathrm{tbl}} \left(m_{\mathrm{tot,ej}}\right)_{\mathrm{tbl}}, \tag{3.16}$$

where $\left(m_{j,0:\mathrm{star}}/m_{\mathrm{tot},0:\mathrm{star}}\right)_{\mathrm{tbl}}$ is the initial mass fraction of element j that was used for the nucleosynthesis calculation. This term, which is often referred to as the yield of element j, will be negative if an element effectively gets destroyed (this is for example the case for hydrogen).

Combining equations (3.14), (3.15), and (3.16), we obtain:

$$\begin{aligned} m_{j,\mathrm{ej}} = {} & \left(m_{j,\mathrm{ej}}\right)_{\mathrm{tbl}} + \\ & \left[\left(\tfrac{m_{j,0:\mathrm{star}}}{m_{\mathrm{tot},0:\mathrm{star}}}\right)_{\mathrm{sim}} - \left(\tfrac{m_{j,0:\mathrm{star}}}{m_{\mathrm{tot},0:\mathrm{star}}}\right)_{\mathrm{tbl}}\right] \left(m_{\mathrm{tot,ej}}\right)_{\mathrm{tbl}}. \end{aligned} \tag{3.17}$$

Note that this expression behaves as expected in the limit that the simulated abundances agree with the ones assumed by the yield tables (i.e. the second term vanishes). Note also that although the abundances appearing in equation (3.17) are absolute, it is the abundance relative to other heavy elements that is important because we interpolate the yield tables to the metallicity (i.e. $\sum_j m_{j,0}/m_{\mathrm{tot},0}$ where the sum is over all elements heavier than helium) of the simulation star particle.

The ejected mass predicted by equation (3.17) can in principle be negative if the simulated relative abundance of some element is much lower than the relative abundance assumed in the yield calculation and if the element is not produced in significant amounts. To prevent stellar particles from obtaining negative total abundances,

[9]Note that this strategy applies directly for our chosen yields since they are presented as what is produced minus what was initially in the star. Some yields (e.g. Woosley & Weaver 1995) would have to be modified to implement this approach.

we therefore impose that for each element j, the *total* ejected mass, which consists of the sum of the mass ejected by intermediate mass stars and SNe of types Ia and II, is non-negative at each time step. If it happens to be negative, we set it to zero. In practice we have, however, not observed this to occur in any of our simulations.

If some $m_{j,\mathrm{ej}}$ has been set to zero, as in the scenario described in the previous paragraph, or if the simulated abundances $(m_{j,0:\mathrm{star}}/m_{\mathrm{tot},0:\mathrm{star}})_{\mathrm{sim}}$ do not add up to unity (which can happen when using smoothed abundances; see section 3.6.2), then the sum of the ejected masses, $\sum_j m_{j,\mathrm{ej}}$, may differ from the total ejected mass, $(m_{\mathrm{tot,ej}})_{\mathrm{tbl}}$, predicted by the yield tables. To ensure that we release the correct amount of mass, we therefore normalise the mass released from each element, including the total metal mass (see section 3.5.1), such that the total mass released agrees with the value found in the yield tables.

Tracking the total metal mass

Of the many elements tracked by stellar evolution calculations, only a fraction contribute significantly to the radiative cooling rates. These elements tend to be the most abundant and thus the most observed. We therefore only track 9 elements individually: H, He, C, N, O, Ne, Mg, Si, and Fe (plus we take Ca and S, whose contributions to the cooling rates can be significant (see chapter 2), to be proportional to Si). Because we only track a finite number of elements, we cannot define the metallicity to be $Z = \sum_j m_j/m_{\mathrm{tot}}$ where the sum is over all elements heavier than He that are tracked by the simulation. Using $Z = 1 - (m_{\mathrm{H}} + m_{\mathrm{He}})/m_{\mathrm{tot}}$ is also problematic since this definition is susceptible to round-off errors.

We therefore treat the total metal mass in the same manner as we treat individual elements, i.e., we include it as an additional array, as has also been done by others (e.g. Lia et al. 2002; Kawata & Gibson 2003; Valdarnini 2003; Sommer-Larsen et al. 2005; Romeo et al. 2006). There are a number of ways to determine the yield of the total metals released by a stellar population, $Y_Z \equiv m_{Z,\mathrm{p:ej}}$. Since the sum of all $Y_j \equiv m_{j,\mathrm{p:ej}}$ (including hydrogen and helium) should be zero (see eq. 3.16), one could simply define $Y_Z = -(Y_{\mathrm{H}} + Y_{\mathrm{He}})$. Unfortunately, yield tables often give $\sum_j Y_j < 0$, which implies that more mass is destroyed than produced. This is mainly due to non-conservation of nucleons and round-off errors (L. Portinari, private communication). We choose therefore to define Y_{Z} as the sum of the yields of all elements heavier than helium and redefine the hydrogen yield as:

$$Y_{\mathrm{H}} \equiv -(Y_{\mathrm{He}} + Y_{\mathrm{Z}}). \tag{3.18}$$

Note that Y_{Z} will differ from the sum of the metal yields of all elements tracked by the simulation if the yield tables contain more elements than are tracked by the simulation. The differences and round-off errors may not be significant in light of the uncertainties in our method (e.g., different yield sets, the definition of metallicity, etc.), but we choose to try to minimize the uncertainties at each step.

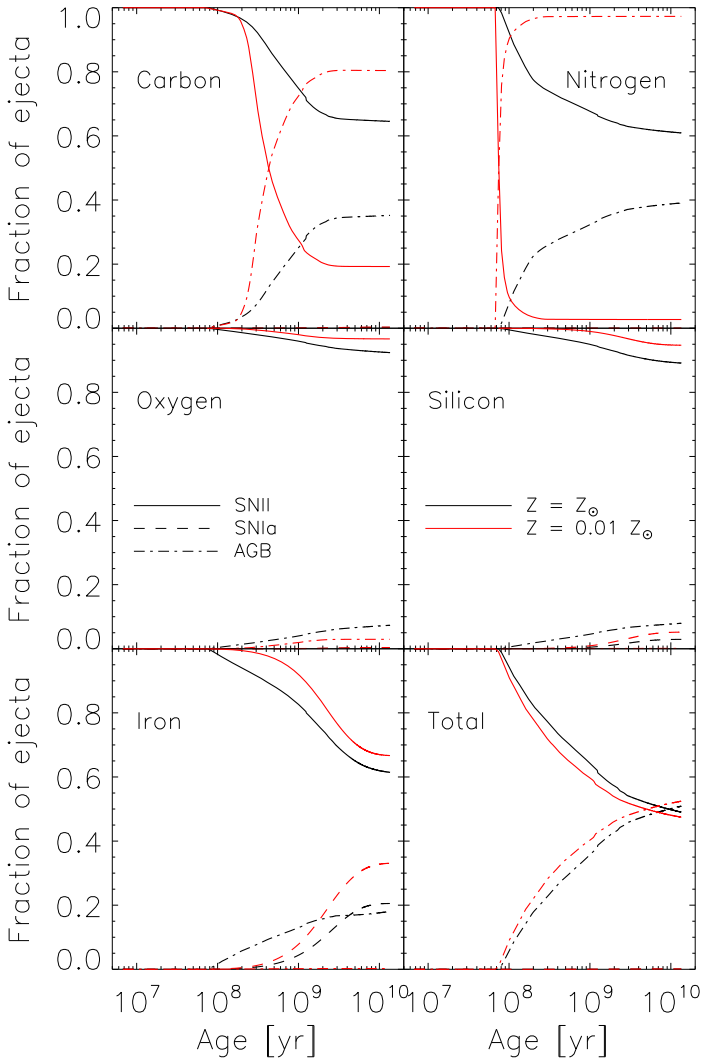

Figure 3.8: The fraction of the integrated mass ejected by an SSP that is due to SNII (solid), SNIa (dashed), and AGB (dot-dashed) as a function of the age of the SSP for two initial stellar metallicities: solar (black) and one per cent of solar (red). All curves assume a Chabrier IMF. The bottom-right panel corresponds to the total ejected mass, whereas the other panels correspond to individual elements, as indicated in the plot. While nearly all the ejecta come initially from SNII, for ages $\tau \gtrsim 10^8$ yr the contributions from AGB stars become significant for carbon, nitrogen and, if the metallicity is high, for other elements as well. The contribution from SNIa very important for iron for $\tau \gtrsim 10^9$ yr. Note that the predictions are uncertain at the factor of two level, mainly due to the freedom in the normalization of the SNIa rate and the uncertainty in the yields.

3.5.2 Results

Figures 3.8 and 3.9 show the result of combining all the ingredients described in section 3.3 using the implementation described in this section. Both figures provide information about the composition of the integrated (i.e., cumulative in time) ejecta of an SSP as a function of its age. While figure 3.8 shows the fraction of the mass due to SNII, AGB and SNIa, figure 3.9 plots the abundance of a few elements relative to iron.

At early times, $\tau \lesssim 10^8$ yr, the integrated ejecta are totally dominated by SNII and consequently the abundances relative to iron of elements such as carbon, nitrogen, oxygen, and silicon are highly supersolar. As the stellar population ages, the contributions of AGB stars become very important for carbon and nitrogen and those of SNIa for iron. Higher initial stellar metallicities tend to result in larger abundances relative to iron, although the effect becomes smaller at late times because the yields of SNIa are independent of metallicity.

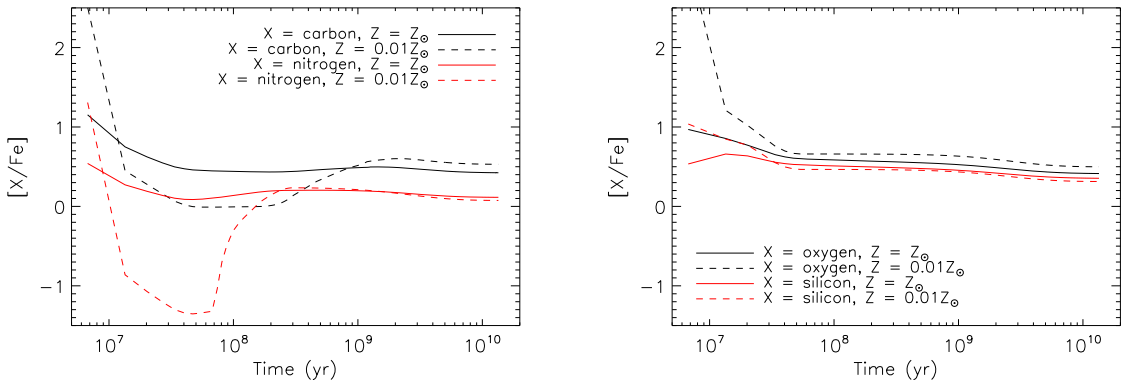

Figure 3.9: The abundances of various elements relative to iron in the integrated ejecta of an SSP as a function of its age for two metallicities: solar (solid) and one per cent of solar (dashed). All curves assume a Chabrier IMF. The abundances of all elements shown are initially enhanced relative to iron, particularly for lower stellar metallicities. The integrated abundances decrease relative to that of iron for $\tau \gtrsim 10^9$ yr when large amounts of iron are ejected by SNIa. Note that the predictions are uncertain at the factor of two level, mainly due to the freedom in the normalization of the SNIa rate and the uncertainty in the yields.

Note that these figures show the properties of the mass released integrated over time rather than at a particular time. For ages $\tau > 10^8$ yr all mass loss comes from AGB stars and SNIa and the elemental abundances relative to iron of the instantaneous ejecta are therefore much lower than those in the integrated ejecta that are shown here.

We emphasize that the predictions shown in these figures are very uncertain, even for a fixed IMF. As we discuss in section 3.3.3, the yields are uncertain at the factor of two level. For example, we rescaled the SNII yields as discussed in section 3.3.3). The relative contribution of SNIa is proportional to the normalization of the SNIa rate, which, as discussed in section 3.3.4, is also highly uncertain. As shown in Fig. 3.8, this is particularly important for iron.

We assumed a Chabrier IMF, but the results presented in this section would be similar for other IMFs as long as they have similar slopes for stellar masses above a few solar masses, as is for example the case for the Salpeter IMF.

3.6 Implementation into SPH

3.6.1 Enrichment scheme

Having determined the ejected masses $m_{j,\mathrm{ej}}$ for each stellar particle during a given time step, we still need to define how much of this mass should go to each of the surrounding gas particles. We would like the mass transfer to be isotropic, but it is not obvious how to accomplish this. As discussed in detail in appendix A of Pawlik &

Schaye (2008), the transport of mass[10] from a source particle to its SPH neighbours is in general highly biased towards the direction of the centre of mass of the neighbours. In essence this is a consequence of the fact that particle-to-particle transport is only possible in directions where there are particles.

Pawlik & Schaye (2008) demonstrate that using an SPH kernel transport scheme, as for example laid out by Mosconi et al. (2001), results in a statistical bias that is much smaller than alternative schemes such as equal weighting or solid angle weighting. It should be noted, however, that while SPH weighting results in only a small statistical bias, the transport from individual source particles is still highly anisotropic. As in previous works (e.g. Steinmetz & Mueller 1994; Kawata 2001; Kawata & Gibson 2003; Tornatore et al. 2004; Scannapieco et al. 2005; Stinson et al. 2006; Kobayashi et al. 2007; Tornatore et al. 2007), we choose to employ SPH weights and transfer to each SPH neighbour k of a given star particle the fraction of the ejected mass given by

$$w_k = \frac{\frac{m_k}{\rho_k} W(r_k, h)}{\sum_i \frac{m_i}{\rho_i} W(r_i, h)}, \tag{3.19}$$

where h is the smoothing length of the star particle (which we determine in the same manner as for gas particles), r_i is the distance from the star particle to neighbour i, W is the SPH kernel, and the sum in the denominator is over all SPH neighbours of the star particle. Tornatore et al. (2007) have investigated changing the number of neighbours and kernel length used for distribution of heavy elements. They found that doubling the amount of neighbours results in an increase of stellar mass fraction by about 10%, presumably because more particles are affected by metal-line cooling. We choose to use 48 neighbours, the same number as is used in the other SPH calculations.

Finally, we note that we do not change the entropy or, equivalently, the internal energy per unit mass of the receiving gas particles. The total internal energy of a receiving particle therefore increases when its mass increases. The thermal energy of the gas surrounding a star undergoing mass loss will change as a result of the mass transfer, but not necessarily by the amount that we implicitly assume. In the case of SN explosions we inject (part of) this energy explicitly (see §3.2) but it is possible that the mismatch of energy could be important. Assuming all star particles lose 100 per cent of their mass and that all this mass is transferred to non-star-forming particles with $T = 10^4\,\mathrm{K}$, the total energy per unit stellar mass that we implicitly use to heat the transferred mass to this temperature is only $(c_\mathrm{s}/v_\mathrm{w})^2/\eta \sim 10^{-4}$ of the kinetic energy released by core collapse SNe, where c_s is the sound speed of the ambient medium. Thus, the energy that we implicitly use in the mass transfer is negligible. Furthermore, many of the receiving gas particles may be star-forming, in which case we impose an effective equation of state (see §3.2).

Similarly, we also neglect the change in the momentum of star particles and their gaseous neighbours as a result of the change in the particle masses. We made this choice partly because we also do not attempt to follow the actual momentum of the ejecta except for core collapse SNe, in which case we inject the kinetic energy explicitly.

[10]Pawlik & Schaye (2008) considered photon transport, but the analysis is equivalent for mass transport.

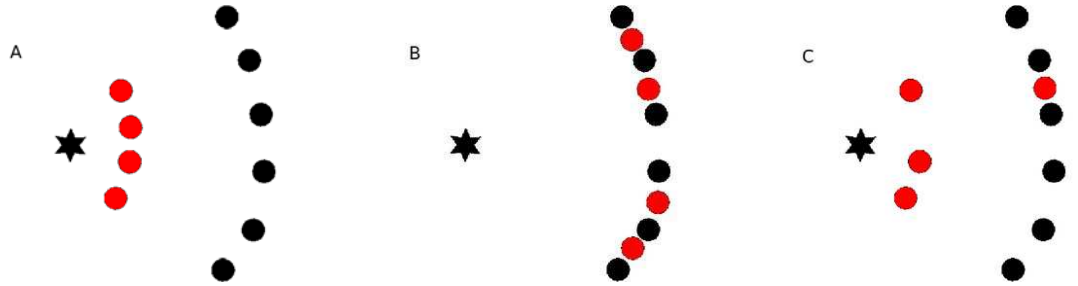

Figure 3.10: The enrichment sampling problem. *A*: A star particle enriches its neighbouring gas particles (red). *B*: The energy released by massive stars within the star particle drives its neighbours away. Because metals are stuck to particle the local metallicity in the shell fluctuates. *C*: Using kinetic feedback the problem is worse because only a small fraction of the neighbours are kicked.

Neglecting momentum transfer from AGB stars and SNIa can be justified for the star particles if the mass transfer is isotropic, which it is in our case. For the receiving gas particles this argument does not apply, even when averaged over many mass transfer events, if the stars and gas have systematically different bulk flows. However, even in that case the energy associated with this momentum transfer is negligible compared with the kinetic energy injected by core collapse SNe unless the bulk flow velocities of the stars differ systematically from those of the gas by $\gtrsim 10^2\,\mathrm{km\,s^{-1}}$.

3.6.2 Smoothed metallicities

The elemental abundances of a particle are not only of interest in the analysis of the simulations, they are also required during the simulation itself because gas cooling rates depend on them. Furthermore, the lifetimes and yields of star particles depend on their metallicities.

Having tracked and transferred the total metal mass released by star particles during all time steps (see section 3.5.1), we could simply define the metallicity of a particle to be

$$Z_{\mathrm{part}} \equiv \frac{m_Z}{m}. \tag{3.20}$$

We will refer to metallicities computed using the above expression as "particle metallicities". Alternatively, we could define the metallicity as the ratio of the SPH smoothed metal mass density and the SPH smoothed gas mass density (as in Okamoto et al. 2005; Tornatore et al. 2007),

$$Z_{\mathrm{sm}} \equiv \frac{\rho_Z}{\rho}, \tag{3.21}$$

where the gas and metal mass densities of particle i are given by the standard SPH expressions

$$\rho_i = \sum_j m_j W(r_i - r_j, h_i), \tag{3.22}$$

$$\rho_{\mathrm{Z},i} = \sum_j m_{\mathrm{Z},j} W(r_i - r_j, h_i), \tag{3.23}$$

where the sum is over all SPH neighbours j and h_i is the smoothing length of particle i. We will refer to metallicities computed using (3.21) as "smoothed metallicities". Similarly, we will make use of particle and smoothed abundances of individual elements. Note that while particle abundances can only change when a particle gains or loses mass, smoothed abundances will generally vary from time step to time step because they depend on the distances between particles and their SPH neighbours. Although most studies do not explicitly define what they mean by "metallicity", particle metallicities are generally used.

The use of smoothed abundances has the advantage that it is most consistent with the SPH formalism. For example, in the absence of metals gas cooling rates depend on ρ and it therefore makes sense for the metallic cooling rates to depend on $\rho_Z \equiv Z_{\mathrm{sm}}\rho$, computed in the same manner as ρ. Another advantage of smoothed abundances is that they partially counter the lack of metal mixing that is inherent to SPH. In particular, there will be many less particles with zero metallicity if smoothed abundances are used because every neighbour of a particle with a non-zero particle metallicity will have a non-zero smoothed metallicity.

The reason SPH underestimates metal mixing is that, in the absence of some implementation of diffusion, metals are stuck to particles. Even in the absence of microscopic diffusion processes, this will result in a lack of metal mixing due to a straightforward sampling problem. This sampling problem is most easily illustrated by imagining a shell of constant thickness swept up by a spherically symmetric explosion driven by a single stellar particle in a uniform, initially primordial gas, just after it has completed the transfer of metals produced by massive stars to its SPH neighbours (see Fig. 3.10). As the metal-rich bubble expands, the local metal density should decrease as $1/r^2$. However, because the metals are stuck to a fixed number of particles, the local metal density will instead fluctuate strongly within the swept-up shell (Fig. 3.10, middle panel). The situation may actually be even worse in practice because we are using kinetic feedback which implies that only a subset of the SPH neighbours of the star particle are kicked (Fig. 3.10, right panel). Note that this sampling problem does not become smaller when the resolution is increased.

The metal sampling problem of SPH can be reduced by implementing diffusion (and tuning the diffusion coefficient). We have, however, decided not to do this because diffusion is a physical process whereas the sampling problem is in essence a numerical problem. Attempting to solve it with a poorly constrained physical mechanism may have undesired consequences. Depending on the severity of the sampling problem, it may for example require an unphysical amount of diffusion. The addition of diffusion may also lead to the introduction of new physical scales (through the choice of a particular value for the diffusion coefficient).

We therefore consider the problem of (turbulent) diffusion separate from the sampling problem described here. While diffusion processes may well be important and have a significant impact on our results (e.g. de Avillez & Breitschwerdt 2007), subgrid recipes are required to implement them as they relevant physical processes are

unresolved in cosmological simulations.

Note that a static gas will not suffer from the sampling problem but diffusion will still alter its metallicity distribution. A possible way out may therefore be to implement a recipe for (turbulent) diffusion that depends explicitly on the relative velocities of neighbouring particles (Greif et al. 2008). Although this will still implicitly use physical processes (e.g. hydrodynamical instabilities) to get around a numerical problem, it does have the important advantage that it asymptotes to the standard, no mixing, solution for the case of a static gas. We intend to test such sub-grid mixing prescriptions in the future. For now, we note that our use of smoothed abundances decreases the severity of – but does not solve – the sampling aspect of the mixing problem, leaving the physical aspect of the problem unaddressed.

We decided to use smoothed abundances in the calculation of the cooling rates, the stellar lifetimes and the yields. When a gas particle is converted into a stellar particle its smoothed abundances are frozen. Note that because the smoothed abundances of gas particles are recalculated at every time step from the metal mass fractions, we need to store both smoothed and particle abundances and can thus compare the two.

It is important to note that metal mass is only approximately conserved when smoothed abundances are used using the "gather approach", equation (3.23). The non-conservation is exacerbated by the fact that the smoothed abundances of a particle are frozen when it is converted from a gas into a star particle. Metal conservation could be enforced by using a "scatter" approach,

$$\rho_{\mathrm{Z},i} = \sum_j m_{\mathrm{Z},j} W'(r_i - r_j, h_j), \tag{3.24}$$

normalized such that $\sum_i W'(r_i - r_j, h_j) = 1$ for every particle j. However, this is computationally more expensive and would in any case only conserve metal mass if the time steps of all particles were synchronized, which is not the case for GADGET.

It is a well known problem that the SPH technique overestimates densities of low density gas in regions where the density gradient is steep, which may result in overcooling (Pearce et al. 1999). By using smoothed metal densities we are vulnerable to a similar problem that may result in an overestimate of the metal mass and hence increased overcooling. Indeed, in our low resolution L025N128 and L100N128 runs the final total smoothed metal masses are, respectively, 3.6% and 18% greater than the final total particle metal masses. However, as expected, the difference decreases rapidly with increasing resolution. For the L100N256, L100N512, and L025N512 runs the total smoothed metal mass is 8.3% higher, 3.7% higher, and 0.14% lower than the total particle metal mass in the respective simulations. Thus, metal mass conservation errors are negligible for our highest resolution simulations.

However, note that we compared total smoothed and particle metal masses in simulations that always used smoothed abundances to compute the cooling rates, stellar lifetimes and yields. Because increased metal abundances will result in increased cooling and thus increased star formation and increased metal production, we expect the difference to increase if we compare the total smoothed metal mass predicted by a simulation employing smoothed abundances with the total particle metal mass pre-

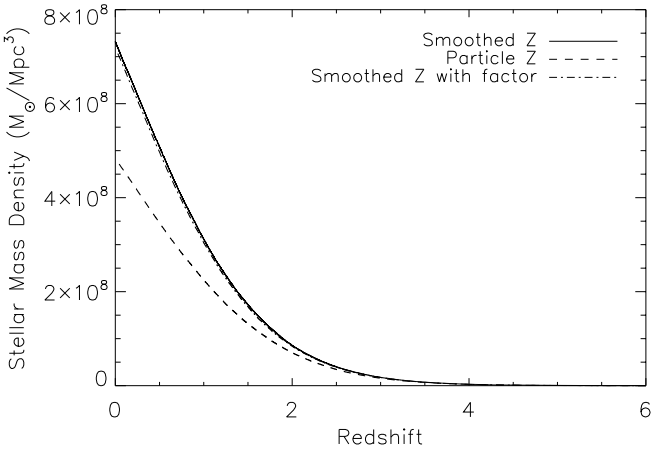

Figure 3.11: Stellar mass density as a function of redshift for 256^3, $100\ h^{-1}\,\mathrm{Mpc}$ runs. The solid curve shows the total stellar mass density in L100N256 which employs smoothed abundances in the calculation of the cooling rates. The dashed curve indicates the total stellar mass in a simulation that used particle abundances for the cooling rates. The use of smoothed abundances increases the stellar mass produced by $z = 0$ by 51 %. The dash-dot curve used smoothed abundances for the cooling after multiplying them by a factor $1/1.08$ to correct for the increase in the total metal mass, at fixed stellar mass, due to the use of smoothed abundances. The fact that the dash-dot curve is close to the black one indicates that the increase in the stellar mass when using smoothed abundances is mostly due to the increased metal mixing rather than the small increase in the total metal mass.

dicted by a simulation employing particle abundances. We have tested this by comparing two L100N256 (and two L100N128) simulations. One simulation used smoothed abundances while the other used particle abundances for the calculation of the cooling rates. Indeed, we found that at $z = 0$ the total smoothed metal mass in the L100N256 (L100N128) simulation using smoothed abundances was 49% (82%) higher than the total particle metal mass in the corresponding simulation using particle abundances.

As can be seen from Figure 3.11, the simulation that uses smoothed abundances (black curve) produces about 1.5 times as many stars as the simulation that used particle abundances (red curve) for the calculation of the cooling rates. We performed a further test to determine if the increase in the stellar mass resulting from our use of smoothed abundances is due to the non-conservation of metal mass or to the increased metal mixing (i.e., metal cooling affects more particles). To this end we ran another version of the L100N256 simulation that used smoothed abundances but in which the smoothed abundances were multiplied by a factor $1/1.08$, which is the ratio between the final total particle and smoothed metal mass in the simulation that used smoothed abundances for the cooling, before passing them to the cooling routine. As can be

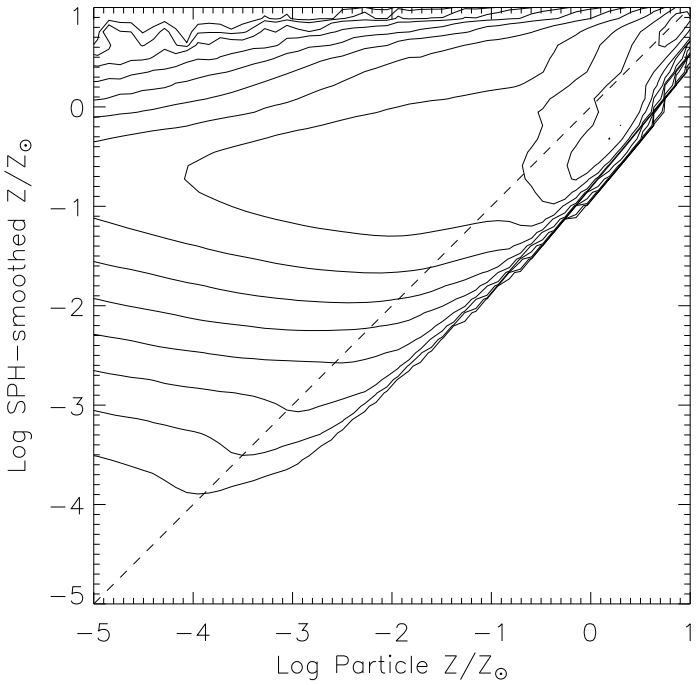

Figure 3.12: Two-dimensional probability density function of particle number density in the smoothed metallicity - particle metallicity plane for the L100N512 simulation at $z = 0$. The contours are spaced logarithmically by 0.5 dex. The two metallicity definitions agree in highly enriched regions where the metals are well mixed, but at lower metallicities the smoothed metallicities are typically higher. The lowest possible smoothed metallicity for a particle with non-zero particle metallicity corresponds to the case when all its neighbours are metal-free and agrees with the lower envelope visible in the plot.

seen from Figure 3.11 (blue curve), the result is much closer to the simulation using smoothed abundances (but without the reduction factor) than to the simulation using particle abundances. Hence, the increase in the total stellar mass is mostly due to the increase in the metal mixing.

This example demonstrates that the poor performance of SPH with regards to metal sampling and mixing is an important problem that can have a very large effect on the predicted star formation history. On the other hand, we expect the differences to be smaller for our higher resolution simulations. The fact that non-conservation of metal mass is much less important than metal mixing and that the mismatch between the total metal masses becomes very small for our highest resolution simulations, support our decision to use smoothed abundances during the simulations. In the rest of this chapter we will therefore only make use of simulations that employed smoothed abundances for the calculation of the cooling rates.

In figure 3.12 we directly compare the $z = 0$ smoothed and particle metallicities in the L100N512 simulation. The contours show the logarithm of the particle number density in the $Z_{\rm sm} - Z_{\rm part}$ plane. The dashed line indicates 1-1 correspondence. The two metallicities are strongly correlated for high metallicities, although significant scatter exists. This is expected, because high-metallicity gas will have been enriched by many star particles during many time steps and we therefore expect the metals to be well mixed. For low particle metallicities, however, the two metallicity definitions become essentially uncorrelated and the smoothed metallicities are typically higher than the particle metallicities. This is because a single enriched particle can give its neighbours a range of smoothed abundances depending on their distances.

For a given particle metallicity, there is a well defined lower limit to the smoothed

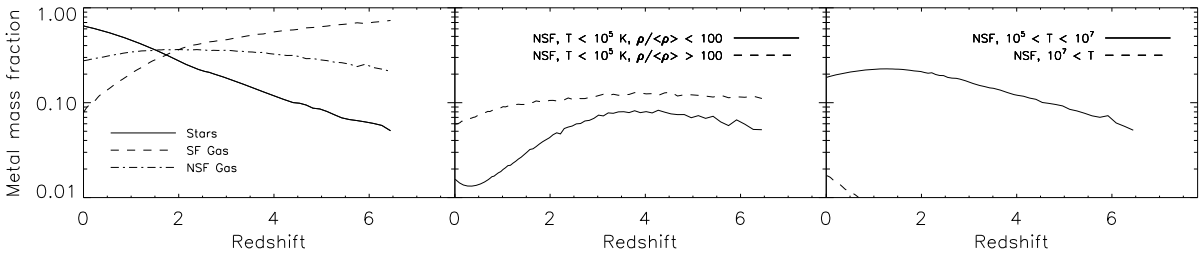

Figure 3.13: Evolution of fractional metal mass in various components for the L100N512 simulation. Left: Stars (solid), star-forming gas (dashed) and non-star-forming gas (dot-dashed). Note that these curves add up to unity. Centre: Cold-warm IGM (non-star-forming, $\rho < 100\langle\rho\rangle$, $T < 10^5\,\mathrm{K}$) (solid), and cold-warm halo gas (non-star-forming, $\rho > 100\langle\rho\rangle$, $T < 10^5\,\mathrm{K}$) (dashed). Right: WHIM (non-star-forming, $T > 10^5\,\mathrm{K}$) (solid) and ICM (non-star-forming, $T > 10^7\,\mathrm{K}$) (dashed). The parts of the curves corresponding to redshifts for which the total metal mass is smaller than 10^{-6} of the total baryonic mass have been omitted because they become very noisy. While most metals initially reside in star-forming gas, by $z = 0$ most are locked up in stars. At present most of the gaseous metals reside in the WHIM.

metallicity. This minimum smoothed metallicity corresponds to that of a metal-bearing particle that is surrounded by metal-free particles. It is visible as the lower envelope of the contours parallel to the dashed line in figure 3.12. From equations (3.21) and (3.23) we can see that the minimum smoothed metallicity is $Z_{\mathrm{sm},i} = m_{\mathrm{Z},i}W(0,h_i)/\rho_i$. Using the fact that for GADGET the value of the kernel at zero displacement is $W(0,h_i) = 8/(\pi h_i^3)$ and that for particles with $m_i \approx m$ the kernel satisfies $4\pi\rho_i h_i^3/3 \approx N_{\mathrm{ngb}}m$ (where the number of SPH neighbours $N_{\mathrm{ngb}} = 48$ in our simulations), it is easy to show that $Z_{\mathrm{sm},i} \approx 2Z_{\mathrm{part},i}/9$.

In summary, we use smoothed abundances during the simulation because it is consistent with the SPH method and because it reduces, though not eliminates, the metal sampling problem. Smoothed and particle metallicities are very close in high-metallicity regions but in low-metallicity regions the smoothed abundances will typically exceed the particle ones. Using SPH simulations to study low-metallicity gas and stars is hence problematic because the results are sensitive to the definition of metallicity that is used. The use of smoothed abundances increases the number of particles for which metal cooling is important and thus the star formation rate, particularly when the resolution is low.

3.7 THE PREDICTED DISTRIBUTION OF METALS

In this section we will investigate the cosmic metal distribution predicted by our simulations. We will only present results from the simulations listed in Table 3.2, which are drawn from the reference simulations of the OWLS set. While the simulations analysed here differ in terms of their box sizes and particle numbers, they all used the same simulation code and the same prescription for star formation, galactic winds and cooling. In chapter 4 we use the full OWLS set to study the effect of changes in the baryonic

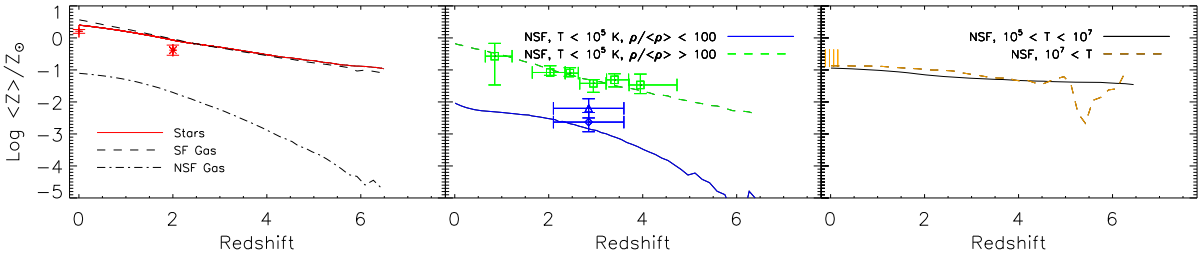

Figure 3.14: Evolution of the mass-weighted metallicities of various components for the L100N512 simulation. The panels and line styles are identical to those shown in Fig. 3.13. The metallicity of stars and the ISM evolves much more weakly than that of cold-warm diffuse gas. The mean metallicity of the WHIM is $\sim 10^{-1}\,Z_{\odot}$ at all times. Symbols indicate observational estimates of metallicities in various phases - stars: (Gallazzi et al. 2008) (plus sign) and (Halliday et al. 2008) (cross symbol); cold halo gas: (Prochaska et al. 2003) (squares); diffuse IGM: (Aguirre et al. 2008) (triangle) and (Schaye et al. 2003) (diamond); ICM: (Simionescu et al. 2009) (orange region).

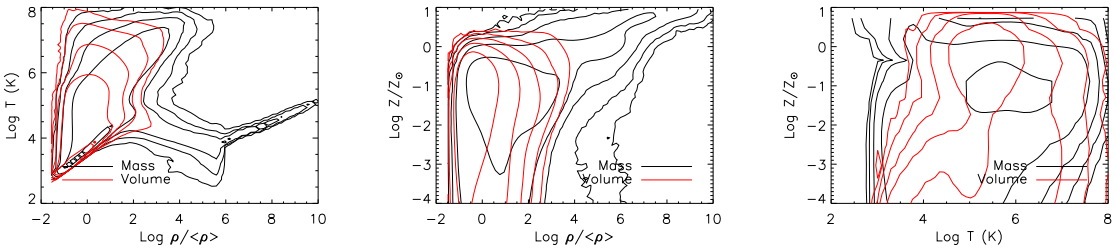

Figure 3.15: Gas distribution weighted by mass (black) and volume (red) in the temperature - density (left), metallicity - density (centre), and metallicity - temperature (right) planes at $z = 0$ for the L100N512 simulation. Note that star-forming gas has been excluded from the right-hand panel. The contours are spaced by 1 dex. While low-density gas displays a wide range of metallicities, there is a strong positive gradient of metallicity with density that becomes narrower for higher densities. Combined with the fact that low-density gas must account for a larger fraction of the volume than the mass, the metallicity-density correlation implies that volume-weighting favors lower metallicities than mass weighting. There is no well defined relation between temperature and metallicity.

processes on the metal distribution, which turns out to be very important. Here we will instead focus on convergence tests and on the effect of different metallicity definitions.

There are a number of approaches we can take to study the cosmic metal distribution in our simulations. Before analysing the metal distribution at $z = 0$ in more detail, we will investigate the evolution of the metal mass fractions in various components. We will then proceed to discuss the dependence of the results on the definition of metallicity (§3.7.1), the size of the simulation box (appendix 3.A) and the numerical resolution (appendix 3.B). While appendices 3.A and 3.B will make use of the full suite of simulations listed in Table 3.2, we will only consider the L100N512 (which contains 2×512^3 particles in a box that is $100\ h^{-1}\,\mathrm{Mpc}$ on a side) run in the rest of this section.

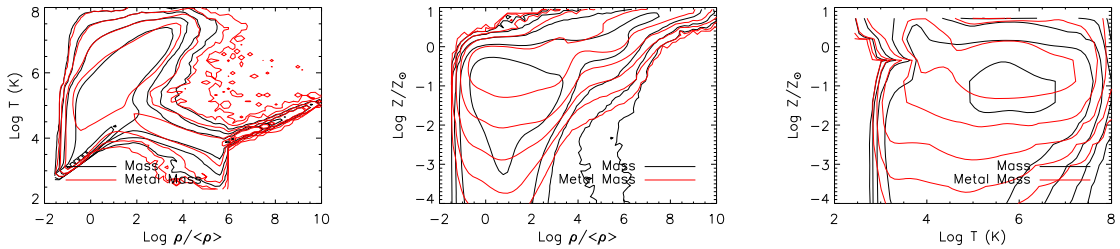

Figure 3.16: Gas mass (black) and gas metal mass (red) distribution in the temperature - density (left), metallicity - density (centre), and metallicity - temperature (right) planes at $z = 0$ for the L100N512 simulation. Note that star-forming gas has been excluded from the right-hand panel. The contours are spaced by 1 dex. While gaseous metals track the general gas mass distribution at high densities (or metallicities), at the densities corresponding to diffuse structures ($\rho \lesssim 10^2 \langle\rho\rangle$) metals reside in gas that is both hotter and more metal-rich than is typical for these densities.

We note, however, that our much higher resolution L025N512 simulation (which was, however, stopped at $z = 1$) gives qualitatively similar results.

Figure 3.13 shows the evolution of the fraction of the metal mass contained in various components. By isolating the gaseous metals into various phases, we can develop a picture of where the metals are at a given redshift. To that end we have plotted the total fraction of the metal mass in stars (left, solid), star-forming gas (left, dashed), and non-star-forming gas (left, dot-dashed). Recall (see §3.2) that by star-forming we mean gas particles that are allowed to form stars and for which we impose an equation of state. These particles all have densities $n_{\rm H} > 10^{-1}\,{\rm cm}^{-3}$ and can be thought of as ISM gas. We have divided the non-star-forming gas into cold-warm ($T < 10^5\,{\rm K}$; middle) and warm-hot ($T > 10^5\,{\rm K}$; right) components. The cold-warm gas has been further subdivided into diffuse ($\rho < 10^2\,\langle\rho\rangle$; middle, solid) and halo ($\rho > 10^2\,\langle\rho\rangle$; middle, dashed) gas and we have subdivided the warm-hot, non-star-forming gas into the warm-hot IGM (WHIM) ($10^5\,{\rm K} < T < 10^7\,{\rm K}$; right, solid), and the intracluster medium (ICM) ($T > 10^7\,{\rm K}$; right, dashed).

Focusing first on the left-hand panel of Fig. 3.13, we see that the most prominent trend is the strong decrease in the fraction of the metals in star-forming gas. While this phase harbors most of the metals at $z = 8$, by $z = 0$ it contains only a small fraction. The opposite is true for the stars: while most of the metals are initially in the gas phase, today the majority of the metals are locked up in stars. The metal fraction contained in non-star-forming gas varies between twenty and forty per cent.

Davé & Oppenheimer (2007) have recently used a cosmological SPH simulation (using 256^3 gas particles in a $32\,h^{-1}\,{\rm Mpc}$ box) to investigate the cosmic distribution of metals. While we postpone a detailed comparison to chapter 4, we note a clear, qualitative difference in the results. While Davé & Oppenheimer (2007) find that initially (at $z = 6$) the diffuse IGM contains much more metal than the ISM, we find the opposite. Schaye et al. (2009) showed this difference mostly reflects the higher initial mass loading of galactic winds assumed by Davé & Oppenheimer (2007). This difference illustrates the importance of varying the subgrid recipes used in the simulations. We

will report on such variations chapter 4.

The other two panels of Fig. 3.13 show that while the metal fraction in cold-warm gas decreases with time, the fraction contained in warm-hot and hot gas increases. This is not unexpected, as growth of structure will result in more and stronger accretion shocks, heating an increasing fraction of the gas to high temperatures. While most of the metals in non-star-forming gas are initially cold, more than half of them reside in the WHIM for $z < 2$. The ICM, on the other hand, still contains only a few percent of the metal mass by $z = 0$, an order of magnitude less than the WHIM.

Besides the metal mass fractions, the metallicities of the various components are also of interest. Together with the evolution of the baryonic mass fractions, which we will present in Dalla Vecchia et al. (in prep), the metallicities determine the metal mass fractions. Figure 3.14 shows the evolution of the mass-weighted mean metallicities of the same components that were shown in Fig. 3.13.

As expected, the metallicity of the star-forming gas roughly traces the metallicity of the stars throughout the simulation, although the ratio of the mean stellar metallicity to the mean ISM metallicity decreases slightly with time. The stellar and ISM metallicities increase relatively slowly with time. At $z = 3$ the mean stellar metallicity is about 0.5 dex lower than at $z = 0$. Interestingly, the WHIM and the ICM have a metallicity $\sim 10^{-1}\, Z_{\odot}$ at all times. This lack of evolution is in stark contrast to the behavior of the cold-warm, diffuse gas whose metallicity increases rapidly with time. Consequently, the differences in the metallicities of the various components become smaller at lower redshifts. However, even by $z = 0$ the metallicity of the diffuse, cold-warm IGM is only of order 1 per cent of solar.

Although our primary aim is not to perform a direct comparison to observations, we have included in Fig. 3.14 a number of observational estimates of metallicity[11] in various phases. In the left panel we show the estimates for the mean stellar metallicity at $z = 0$ and $z = 2$ from Gallazzi et al. (2008) and Halliday et al. (2008), respectively. Our simulations fall about 0.2 dex above the redshift zero point and land about 0.3 dex above the higher redshift point. We note however, that Halliday et al. (2008) find their result to be low compared to that of Erb et al. (2006). They explained that this could represent an alpha enhancement at high redshift (Erb et al. 2006 measured oxygen while Halliday et al. 2008 measured iron). We compare our predictions for overdense, cold, non-starforming gas to the observations of damped Lyα (DLA) systems of Prochaska et al. (2003) and find excellent agreement. Our measurement of the mean metallicity of the $z \approx 3$ IGM agrees with the measurement based on carbon of Schaye et al. (2003), but falls slightly below that based on oxygen of Aguirre et al. (2008). In appendix 3.B we show that the metallicity of this phase is particularly sensitive to resolution and that higher resolution simulations may predict higher diffuse IGM metallicities. Finally, the metallicity of the low-redshift ICM falls along the lower range of cluster measurements compiled by Simionescu et al. (2009). For this we compiled a range of all metallicity measurements in the most outer regions of the clusters (regions which should dominate the mass averaged metallicity). We note that since most radial profiles flatten at outer radii, this should be a safe assumption. From these comparisons we conclude

[11] The observations were converted to our solar abundances where necessary.

that our simulation is in reasonable agreement with a range of observations. Although these values for mean metallicity are often luminosity weighted, we wish to avoid for now further uncertainties introduced by modelling the emission so we simply compare with our mass-weighted values.

Before investigating the robustness of these results to numerical effects, we will study the $z = 0$ metal distribution in more detail. To interpret the results, it is, however, helpful to first consider the gas mass rather than the metal mass distribution.

The solid contours in the left-hand panel of figure 3.15 indicate the $z = 0$ gas mass-weighted 2-dimensional (2-D) probability density function (PDF) in the temperature-density plane. That is, the contour values correspond to $dM_{\rm g}/(M_{\rm g,tot} d\log\frac{\rho}{\langle\rho\rangle} d\log T)$. Similarly, the red contours show the volume-weighted[12] 2-D PDF, i.e., $dV/(V_{\rm tot} d\log\frac{\rho}{\langle\rho\rangle} d\log T)$. All contour plots in this section show contours spaced by one dex, with each plot containing the same levels for both linestyles.

There are a number of distinct features in this temperature-density diagram. Much of the mass, and nearly all of the volume, resides in a narrow strip ranging from about $(\log\rho/\langle\rho\rangle, \log T) \sim (-1.5, 3)$ to $\sim (1.5, 4.5)$, which corresponds to the diffuse, photo-ionized IGM. The relation between temperature and density of this component is set by the balance between photo-heating and adiabatic cooling (Hui & Gnedin 1997). For gas at higher overdensities photo-heating is balanced by radiative rather than adiabatic cooling and the temperature slowly decreases with increasing density. The plume of much hotter gas corresponds to gas that has been shock-heated, either through gravitationally induced accretion shocks or galactic winds. For gas with densities $\rho/\langle\rho\rangle \gtrsim 10^2$ there is less mass at temperatures $T \sim 10^5\,{\rm K}$ than there is at lower and higher temperatures because the radiative cooling rates peak at these temperatures (due mostly to collisional excitation of oxygen, carbon, and helium), resulting in a bimodal distribution of the temperature in that density regime. The well-defined T-ρ relation at the highest densities reflects the equation of state $P \propto \rho_g^{4/3}$, which we impose on gas with densities exceeding our star formation threshold of $n_{\rm H} = 0.1\ {\rm cm}^{-3}$ ($\rho/\langle\rho\rangle \sim 10^6$ at $z = 0$). As discussed in §3.2, the temperature of this gas merely reflects the imposed effective pressure of the unresolved multiphase ISM.

The middle and right panels of Fig. 3.15 show how the gas mass (black) and the volume (red) are distributed in the metallicity-density and the metallicity-temperature planes, respectively. We have excluded star-forming gas from the right-hand panel since its temperature would merely reflect the pressure of the equation of state that we have imposed. We will exclude this component from all plots investigating temperature dependencies, except for temperature-density diagrams such as the left-hand panel of Fig. 3.15 (because in that case the gas density can be used to identify the star-forming gas).

While there is a clear positive correlation between metallicity and density for highly overdense gas (see the black contours in the middle panel), gas at low overdensities can have a large range of metallicities extending all the way to zero (outside the plotted range). Note that the highest density gas is highly supersolar. This reflects the fact that

[12]Volume weighting was implemented as weighting by $h_i^3/\sum_j h_j^3$, where h_i is the SPH smoothing length of particle i. We verified that using m/ρ instead of h^3 gives nearly identical results.

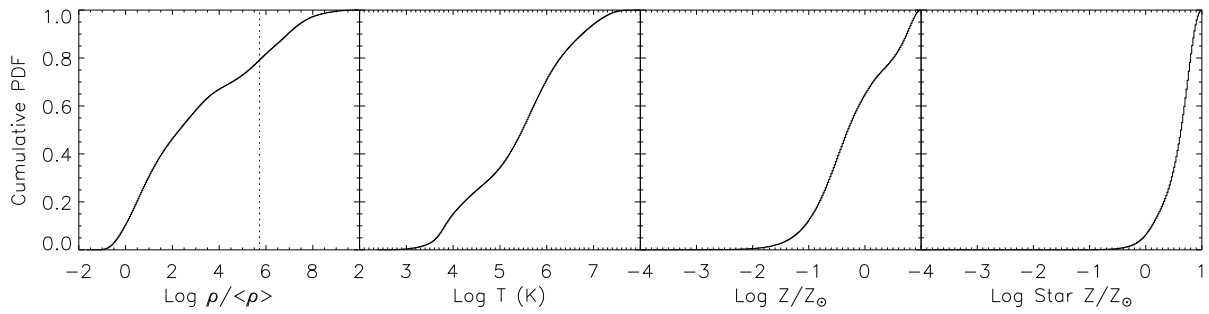

Figure 3.17: Cumulative probability density function of the gas metal mass as a function of gas density (*left*), temperature (*centre-left*), and metallicity (*centre-right*) at $z = 0$ for the L100N512 simulation. The vertical, dotted line in the left panel indicates our star formation threshold. Also note that star-forming gas has been excluded from the temperature plot. The right-hand panel shows the cumulative PDF of the stellar metal mass as a function of the stellar metallicity. While the gas metal mass is distributed over a wide range of densities and temperatures, it is concentrated in gas that has a relatively high (local) metallicity.

massive galaxies in this simulation have too high metallicities because galactic winds cannot escape their high-pressure ISM. In chapter 4 we will show that this problem is not present for some other implementations of galactic winds driven by SNe and, particularly, for more efficient feedback mechanisms such as energy injected by active galactic nuclei. The right-hand panel shows that there is no well-defined relation between metallicity and temperature. Gas at a given temperature displays a wide range of metallicities.

Figure 3.16 uses the same panels as Fig. 3.15 to compare the distribution of gas mass (black) and metal mass (red). Since we use smoothed metallicities, metal mass is defined as $Z_{\rm sm}M_{\rm g}$. Note that the black contours are identical to those shown in Fig. 3.15. Focusing first on the left-hand panel, which shows the distributions in the temperature-density plane, we see that while metal and gas mass track each other well for high overdensities (although the gas mass is distributed over a narrower range of temperatures for a given density), they differ in one important respect for $\rho/\left\langle\rho\right\rangle \lesssim 10^2$. Whereas most of the mass is concentrated at the lowest densities and temperatures, this diffuse, photo-ionized IGM contains only a small fraction of the metals. Instead, the vast majority of metals in low-density gas are hot ($T \gtrsim 10^5$ K). This is probably caused by the fact that high-velocity winds are required to transport metals to regions far from galaxies and that such winds shock-heat the medium. This agrees with Theuns et al. (2002) and Aguirre et al. (2005), who also found that most of the diffuse metals reside in hot gas, using different implementations of feedback from star formation and using simulations that did *not* include metal-line cooling. Aguirre et al. (2005) speculated that the inclusion of radiative cooling by metals might be important, but our simulations show that even when metal-line cooling is included, the WHIM ($5 < \log T < 7$, $\rho/\left\langle\rho\right\rangle \lesssim 10^3$) is an important reservoir of cosmic metals. From the right-hand panel of Fig. 3.15 we can see that although some WHIM gas has very low metallicities, much of it has $Z \gtrsim 10^{-1}\ Z_{\odot}$.

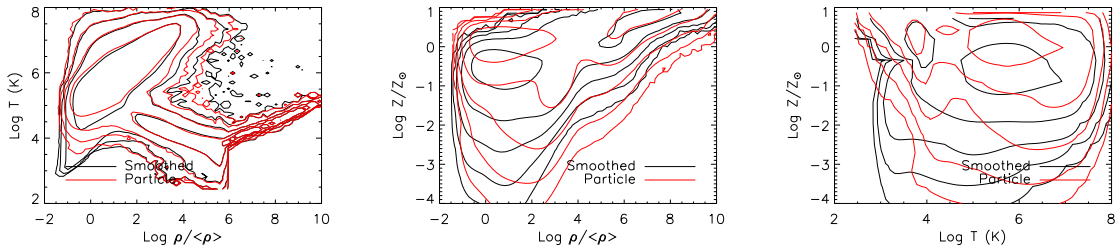

Figure 3.18: Gas smoothed metal mass (black) and gas particle metal mass (red) distribution in the temperature - density (left), metallicity - density (centre), and metallicity - temperature (right) planes at $z = 0$ for the L100N512 simulation. Note that star-forming gas has been excluded from the right-hand panel. The contours are spaced by 1 dex. Except for low-metallicity gas, which mostly has low densities and temperatures, smoothed and particle metallicities yield similar results.

The left-hand panel of Fig. 3.17 shows the cumulative PDF for the gas metal mass as a function of $\log \rho / \langle\rho\rangle$, i.e., $\frac{1}{M_{\mathrm{Z_{sm,tot}}}} \int_0^\rho d\rho' \frac{d(M_{\mathrm{g}} Z_{\mathrm{sm}})}{d\rho'}$, where $M_{\mathrm{Z_{sm,tot}}}$ is the total smoothed metal mass in gas. Similarly, the second and third panels from the left show the cumulative PDF of the gas metal mass as a function of temperature and metallicity and the right-hand panel shows the cumulative PDF of the stellar metal mass as a function of metallicity. While the gas metal mass is spread over remarkably large ranges of densities and temperatures, it is concentrated in relatively high-metallicity gas. Note, however, that metallicity is evaluated locally, at the resolution limit of the simulation. High metallicity gas therefore includes patches of enriched gas embedded in structures whose overall metallicity is low.

Considering one variable at a time, ninety percent of the $z = 0$ gas metal mass resides in gas with $10^{-0.5} \lesssim \rho / \langle\rho\rangle \lesssim 10^{7.5}$, $10^4\,\mathrm{K} \lesssim T \lesssim 10^{6.5}\,\mathrm{K}$, or $10^{-1.5} \lesssim Z_{\mathrm{sm}}/Z_\odot \lesssim 10^{0.7}$. Half the gaseous metal mass resides in gas with $\rho < 10^2 \langle\rho\rangle$ which implies that diffuse and collapsed structures contain similar amounts of metal mass. In terms of temperature the midpoint lies at about 10^5 K, which means that half the gas metal mass resides in shock-heated gas. Clearly, any census aiming to account for most of the metal mass in gas will have to take a wide variety of objects and structures into account.

In the next section we will investigate the metal distribution and its evolution in more detail, including the sensitivity of the results to the definition of metallicity. The convergence of the predictions with respect to the size of the simulation box and the numerical resolution is studied in appendices 3.A and 3.B, respectively.

3.7.1 Smoothed vs. particle metallicity

As discussed in §3.6.2, there is some ambiguity in the definition of the metallicity in SPH. We have opted to use SPH smoothed metallicities $Z_{\mathrm{sm}} \equiv \rho_Z/\rho$ rather than particle metallicities $Z_{\mathrm{part}} \equiv m_Z/m$, because using smoothed abundances is consistent with the SPH method and because it partially counters the lack of metal mixing that results

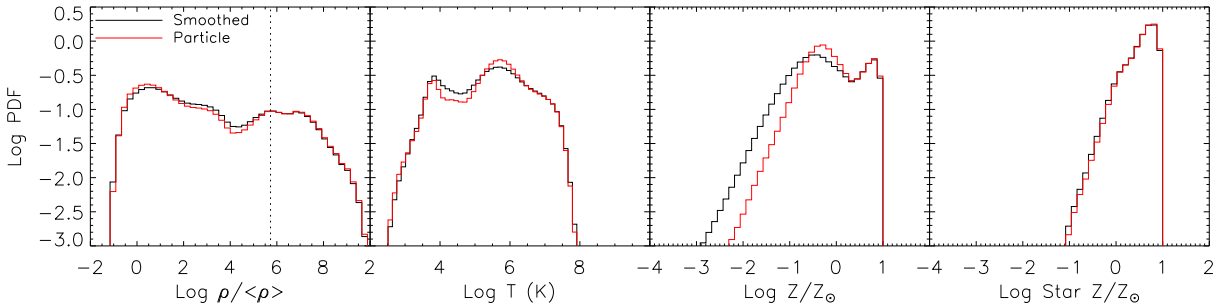

Figure 3.19: Probability density function of the gas density (left), temperature (centre-left) and smoothed/particle metallicity (centre-right) weighted by smoothed (black) and particle (red) metal mass. The black (red) histogram in the right-hand panel shows the PDF of the smoothed (particle) stellar metallicity weighted by smoothed (particle) metal mass. All panels correspond to the L100N512 simulation at $z = 0$. The vertical, dotted line in the left panel indicates the threshold for star formation. Note that star-forming gas was excluded from the temperature panel. The predictions for smoothed and particle metallicities only differ significantly for low-metallicity gas.

from the fact that metals are stuck to particles. We already demonstrated in §3.6.2 that the definition of metallicity is particularly important for low metallicity gas and that it has important consequences for gas cooling rates (and hence for the predicted star formation histories). Here we investigate its effect on the metal distribution by comparing the gas metal mass distributions computed using smoothed and particle metallicities. Note, however, that smoothed metallicities were always used during the simulation for the calculation of the radiative cooling rates, stellar lifetimes, and stellar yields.

Figure 3.18 compares the gas metal mass distribution using smoothed (black) and particle (red) metallicities in the temperature-density (left), metallicity-density (middle) and metallicity-temperature (right) planes. Note that the black contours are identical to the red contours in Fig. 3.16. The smoothed and particle metal distributions trace each other reasonably well, except for the diffuse, photo-ionized IGM ($\rho/\langle\rho\rangle < 10^2$, $T < 10^5\,\mathrm{K}$; left panel) and generally for low-metallicity gas ($Z \ll Z_\odot$; middle and right panels). When smoothed metallicities are used larger fractions of the metal mass reside in low-metallicity gas, which is consistent with Fig. 3.12.

The left-hand panel of figure 3.19 shows the 1-D gaseous metal mass weighted PDF for the gas density, i.e., $d(M_\mathrm{g}Z)/(M_{Z,\mathrm{tot}}d\log\frac{\rho}{\langle\rho\rangle})$ as a function of $\log\rho/\langle\rho\rangle$, where Z is the smoothed/particle metallicity and $M_{Z,\mathrm{tot}}$ is the total smoothed/particle metal mass in gas. Thus, if the y-axis were linear (which it is not), the fraction of the area underneath the histogram that is in a given bin would correspond to the fraction of the gas metal mass in that bin. Similarly, the second and third panels from the left show the metal-mass weighted PDF of the temperature and metallicity, respectively, and the right-hand panel shows the metal mass-weighted PDF of the stellar metallicity. The distribution of metal mass over density is similar for smoothed and particle metallicities, but using smoothed metallicities results in a significant shift of metal mass from $T \sim 10^6\,\mathrm{K}$ to $T < 10^5\,\mathrm{K}$. While the differences in the metal distributions as a function

of metallicity are small for stars, presumably because they tend to form in well-mixed, high density gas, the differences are very substantial for the gas. As expected, the use of smoothed metallicities results in a prominent shift of gaseous metal mass to lower metallicities. For stars, the particle metallicity PDF exceeds that for smoothed abundances by about an order of magnitude in the range $-4 < \log Z < -2$ (i.e., outside the plotted range).

We stress, however, that because the metallicities are evaluated locally, i.e. at the spatial resolution limit, they may differ substantially from the overall mean metallicity of the structure containing the particles. For structures that contain many particles the mean metallicity will be insensitive to the definition of metallicity that is used. On the other hand, local gas metallicities are the ones that are used for the calculation of the cooling rates, so they are certainly important.

In summary, SPH simulations such as the ones presented here are not well-suited to study the metal distribution in low-metallicity gas. Because metals are stuck to particles, SPH suffers from a sampling problem which becomes worse in regions where only a small fraction of the particles have been enriched. Consequently, in the low-metallicity regime the distribution of mass is sensitive to the definition of metallicity. However, the bulk of the metals reside in gas of relatively high metallicity for which the predicted metal distribution is not strongly affected by the lack of metal mixing. Except for the small fraction of stars that have $Z \lesssim 10^{-1}\, Z_{\odot}$, the results are more robust for stars because they form in high-density gas that is better mixed. This is probably because high-density gas particles tend to be near star particles which means that they are likely to have received metals during many time steps.

3.8 Summary

The elemental abundances of stars, galaxies, and diffuse gas are of great interest because they determine radiative cooling rates and the stellar initial mass function, because they can give insight into physical processes such as the interactions between galaxies and the IGM, because they change the strength of lines that are used as diagnostics of physical conditions and because they determine the observability of lines used as tracers of various gas phases. In this chapter we have presented a method to follow the timed release of individual elements by stars, including mass loss through stellar winds and SNe, and their subsequent dispersal through space.

The ingredients of our stellar evolution module include a choice of IMF (we use Chabrier), stellar lifetimes as a function of metallicity (which we take from Portinari et al. 1998), the rate of type Ia SNe for an SSP as a function of time (we use an empirical time delay distribution tuned to obtain agreement between the evolution of the observed, cosmic rates of SNIa and star formation), and stellar yields (we use Marigo 2001 for AGB stars, Portinari et al. 1998 for core collapse SNe, and the W7 model of Thielemann et al. 2003 for SNIa).

We compared different sets of nucleosynthetic yields taken from the literature after integrating them over the IMF. While the different studies predict similar total ejected masses, the predictions for heavy elements differ substantially. In particular,

the ejected masses of individual elements differ by factors of a few for AGB stars and – for elements heavier than nitrogen – for core collapse SNe. Thus, even disregarding the fact that most nucleosynthetic yield calculations ignore potentially important effects such as rotation, the elemental ratios are uncertain by factors of a few for a fixed IMF. Predictions for abundances relative to iron are even less robust because much, perhaps even most, of the iron released by an SSP is produced by SNIa and the normalization of the SNIa rate is only known to within factors of a few.

Our implementation of mass transfer implicitly splits, for each element, the ejected mass into terms accounting for the mass that is produced (minus destroyed) and the mass that is simply passing through. The latter term is assumed to scale with the initial abundance, allowing us to correct for relative abundance variations with respect to solar at a fixed metallicity.[13] We have taken special care to correctly track the total metal mass even if not all elements are tracked explicitly.

We discussed two possible definitions of metallicity of SPH particles: the commonly used "particle metallicity", defined as the ratio of the metal to the total mass (m_Z/m), and the "smoothed metallicity", defined as the ratio of the metal mass density to the total mass density (ρ_Z/ρ), where each density is computed using the standard SPH formalism. We argued that smoothed metallicities (and, analogously, smoothed elemental abundances) are preferable because they are most consistent with the SPH formalism (particularly with regards to radiative cooling rates which depend explicitly on densities) and because they partially counter the lack of metal mixing that is inherent to SPH. We discussed in some detail the fact that SPH underestimates metal mixing because metals are stuck to particles and how this results in a sampling problem that may not become smaller when the resolution is increased. While the use of smoothed abundances eases this problem somewhat, it by no means eliminates it entirely (while also leaving the potential for small scale metal mixing due to physical processes unaddressed).

The use of smoothed abundances (which are frozen when a gas particle is converted into a star particle) leads to a slight non-conservation of metal mass, but we showed this to be negligible for our high-resolution simulations. A comparison of smoothed and particle metallicities (in a simulation that used smoothed abundances for the cooling rates and the stellar evolution) shows that while they are similar at high metallicities, they differ strongly at low metallicities, with smoothed abundances typically exceeding particle abundances by large factors. In particular, there are many more particles with non-zero smoothed metallicities than with non-zero particle metallicities. Since there is no overwhelming reason to prefer one definition of metallicity over the other, the fact that the choice matters indicates that care must be taken when interpreting the predictions of SPH simulations at low metallicities.

A comparison between two low-resolution simulations, one using smoothed abundances and the other using particle abundances for the calculation of the cooling rates, revealed large differences in the star formation rate. By redshift zero the simulation employing smoothed abundances had formed about 1.5 times as many stars as the

[13] Note that this treatment still ignores the fact that the nucleosynthesis may itself depend on the relative abundances.

run using particle metallicities. We demonstrated that this difference could not be attributed to non-conservation of metal mass and was instead caused by the increased mixing (i.e., metal cooling is important for more particles when smoothed abundances are used). Although the difference is expected to decrease with increasing resolution, we conclude that it will be necessary to solve the metal mixing problem before SPH simulations can be used to make precise predictions for the cosmic star formation rate.

We used a suite of large simulations with up to 2×512^3 particles to investigate the distribution of heavy elements. All simulations used identical physical parameters and sub-grid modules. The simulations made use of recently developed modules for star formation (Schaye & Dalla Vecchia 2008) and kinetic feedback from core collapse SNe (Dalla Vecchia & Schaye 2008). We followed all 11 elements (H, He, C, N, O, Ne, Mg, Si, S, Ca, Fe) that we found in chapter 2 to contribute significantly to the cooling of photo-ionized plasmas. Radiative cooling (including photo-heating) was implemented element-by-element, assuming the gas to be optically thin and in ionization equilibrium in the presence of an evolving photo-ionizing radiation background. We did this by making use of tables that had been pre-computed using CLOUDY following the methods in chapter 2. Element-by-element cooling and the inclusion of photo-ionization – not only for H and He, but also for heavy elements – are both novel features for cosmological simulations.

Our predictions for the metallicities of various baryonic phases are in reasonably good agreement with available observations. While most of the cosmic metal mass initially resides in gas of densities typical of the ISM ($n_{\rm H} > 10^{-1}\,{\rm cm}^{-3}$), by redshift zero stars have become the dominant reservoir of metal mass and the ISM contains only a small fraction of the metals. Diffuse gas ($n_{\rm H} < 10^{-1}\,{\rm cm}^{-3}$) contains a significant fraction of the metals at all times. Except at very high redshifts, most of the diffuse metals reside in the WHIM ($10^5\,{\rm K} < T < 10^7\,{\rm K}$), but the metal mass residing in the ICM ($T > 10^7\,{\rm K}$) is always negligible. By the present time, the gaseous metal mass is distributed over a wide range of densities (5, 50, and 95 per cent of the metal mass resides in gas with $\rho/\langle\rho\rangle \lesssim 10^{-0.5}$, 10^2, and $10^{7.5}$, respectively) and temperatures (5, 50, and 95 per cent of the metal mass resides in gas with $T\,({\rm K}) \lesssim 10^4$, 10^5, and $10^{6.5}$, respectively), but is concentrated in gas that has a relatively high, local metallicity (95 per cent has $Z \gtrsim 10^{-1.5}\,Z_\odot$ averaged over the mass scale corresponding to the resolution limit). Clearly, any census aiming to account for most of the metal mass will have to take a wide variety of objects and structures into account.

Although the mean stellar metallicity slowly increases with time, it is already of order ten per cent of solar by $z = 8$. The evolution of the metallicity is much stronger for cold-warm ($T < 10^5\,{\rm K}$) diffuse gas, particularly for $\rho/\langle\rho\rangle < 10^2$. By redshift zero the diffuse, photo-ionized IGM has a metallicity $\sim 10^{-2}\,Z_\odot$, while the cold-warm gas in halos has $Z > 10^{-1}\,Z_\odot$. Interestingly, the metallicity of the WHIM and the ICM is $\sim 10^{-1}\,Z_\odot$ at all redshifts.

A comprehensive convergence study (see appendices 3.A and 3.B) revealed that, except for the ICM, a $50\,h^{-1}\,{\rm Mpc}$ box is sufficiently large to obtain a converged result for the cosmic metal mass fractions and metallicities down to $z = 0$ and $12.5\,h^{-1}\,{\rm Mpc}$ suffices for $z > 2$. The convergence with respect to numerical resolution was consistent

with expectations based on a comparison with the Jeans scales. Our use of an effective equation of state for star-forming gas guarantees that the Jeans mass does not fall below $f_{\rm g}^{3/2} 10^7\, h^{-1}\,{\rm M}_\odot$, where $f_{\rm g}$ is the local gas fraction, but even this scale is only marginally resolved in our highest resolution simulations (which have $m_{\rm g} \sim 10^6\, h^{-1}\,{\rm M}_\odot$). We found that it is much easier to obtain converged predictions for the metallicity of the different components than for their metal mass fractions. While the simulations presented here can provide (numerically) robust predictions for the metallicities at $z < 4$, higher resolution models may be required for higher redshifts.

Here we have investigated only a single set of physical parameters. We postpone such a comparison to chapter 4 that will investigate how the predictions for the metal distribution vary if we change the physical assumptions and sub-grid prescriptions, such as the cosmology, the star formation recipe, the implementation and efficiency of galactic winds, the cooling rates, and feedback from AGN. In this way we hope to isolate the processes that drive the evolution of the cosmic metal distribution.

Acknowledgments

We are grateful to Volker Springel for help with the simulations and to Laura Portinari and Robert Izzard for discussions about stellar yields. We are also grateful to Stefano Borgani, Andreas Pawlik, and the anonymous referee for their careful reading of the manuscript. This work was supported by Marie Curie Excellence Grant MEXT-CT-2004-014112.

3.A Varying the size of the simulation box

In this appendix we use the suite of cosmological simulations listed in Table 3.2 to test for convergence with the size of our simulation box. The size of the simulation box is important because it determines what kind of objects can form. Rare, large-scale structures (both high- and low-density peaks) can obviously only be sampled correctly if they are much smaller than the size of the box. Moreover, since Fourier components of the density field only evolve independently in the linear regime, the simulation box must be large compared with the scale that has last gone non-linear. Because this scale increases with time, larger boxes are required at lower redshifts. To isolate the effect of the size of the simulation volume, we will compare simulations that use different box sizes, *while holding the resolution constant*.

For this test we use two sets of simulations that differ in terms of their resolution. The first set consists of L100N512, L050N256, and L025N128 and the second set comprises L025N512, L012N256, and L006N128. Within each set the size of the box is thus decreased by factors of two and four, respectively. The second set uses a particle mass that is 64 times smaller than the first set, but these higher resolution runs were not continued down to $z = 0$.

The top and bottom rows of figure 3.20 show the evolution of the metal mass fractions in the various components for the low and high-resolution sets, respectively. The

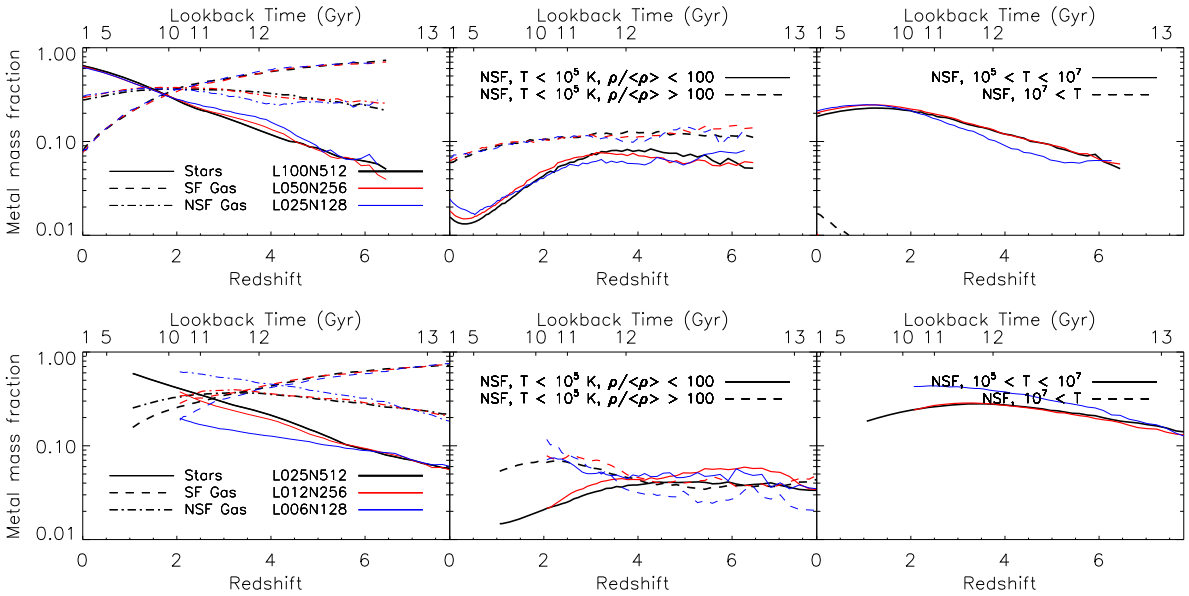

Figure 3.20: Dependence on the simulation box size of the evolution of the fractions of the metal mass in various components. The curves in the top panels correspond to the L100N512 (black), L050N256 (red), and the L025N128 (blue) simulations. The curves in the bottom panels are for the L025N512 (black), L012N256 (red), and the L006N128 (blue) simulations. The line styles are identical to those shown in Fig. 3.13. The parts of the curves corresponding to redshifts for which the total metal mass is smaller than 10^{-6} of the total baryonic mass have been omitted because they become very noisy. Except for the ICM ($T > 10^7$ K), the $50\ h^{-1}\,\mathrm{Mpc}$ and $12.5\ h^{-1}\,\mathrm{Mpc}$ boxes have nearly converged for $z < 2$ and $z > 2$, respectively.

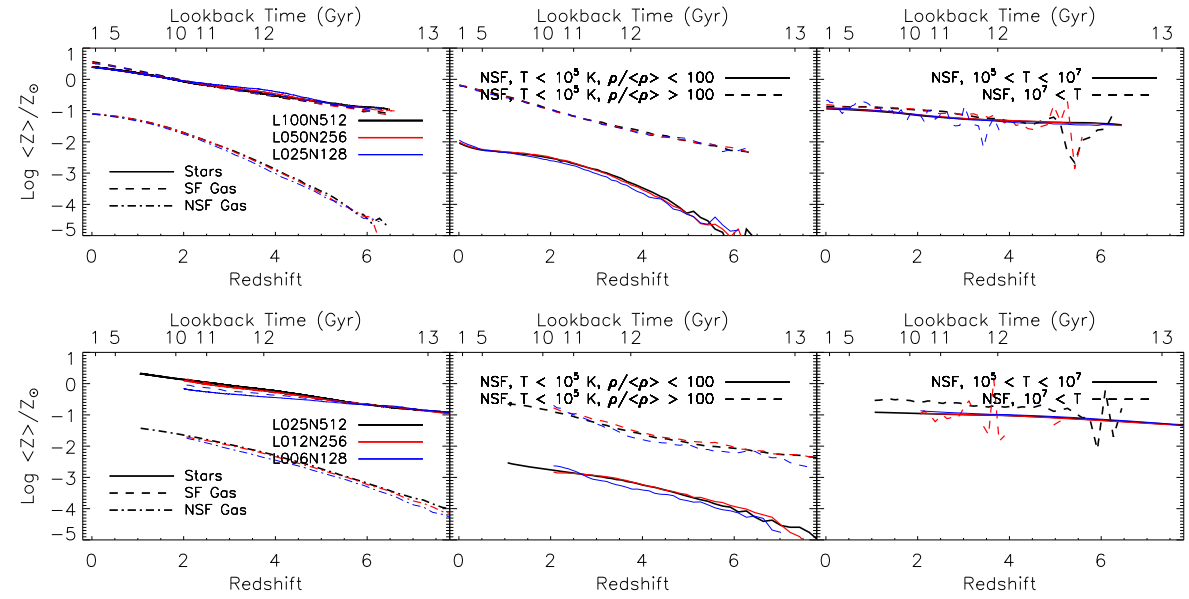

Figure 3.21: Dependence on the simulation box size of the evolution of the metallicities of various components. The colors and line styles are identical do those used in Fig. 3.20. The $25\ h^{-1}\,\mathrm{Mpc}$ and $12.5\ h^{-1}\,\mathrm{Mpc}$ boxes have converged for $z < 2$ and $z > 2$, respectively.

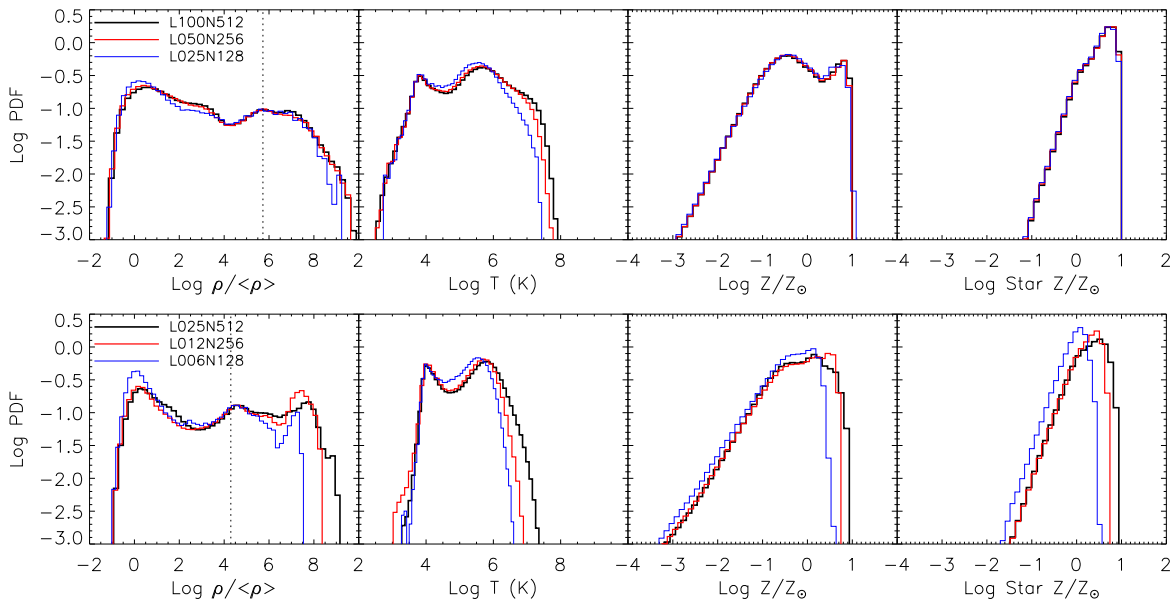

Figure 3.22: Dependence on the size of the simulation box of the probability density function, weighted by metal mass, of the gas density (left), temperature (centre-left), gas metallicity (centre-right), and stellar metallicity (right) at $z = 0$ (top) and $z = 2$ (bottom). The colors and line styles are identical to those used in Fig. 3.20. The vertical, dotted lines in the left panels indicate the threshold for star formation. Note that star-forming gas was excluded from the temperature panels. Except for the extremes of the distributions, the $50\ h^{-1}\,\mathrm{Mpc}$ and $12.5\ h^{-1}\,\mathrm{Mpc}$ boxes have nearly converged for $z < 2$ and $z > 2$, respectively.

panels are analogous to those shown in Fig. 3.13. In particular, the black curves in the top panels, which correspond to L100N512, are identical to those shown in Fig. 3.13. The top panels demonstrate that, except for the $T > 10^5\,\mathrm{K}$ gas (right panel), the results have already nearly converged for the $25\ h^{-1}\,\mathrm{Mpc}$ box. For the WHIM (right; solid) we require a $50\ h^{-1}\,\mathrm{Mpc}$ box, although even the $25\ h^{-1}\,\mathrm{Mpc}$ box seems to be nearly converged for $z < 2$. For the ICM (right; dashed), however, even the $50\ h^{-1}\,\mathrm{Mpc}$ box is too small. The bottom panels demonstrate that while a $12.5\ h^{-1}\,\mathrm{Mpc}$ box is sufficient for $z > 2$ (except for the ICM, which accounts for too few metals to be visible in the plot, and the photo-ionized IGM), boxes as small as $6.125\ h^{-1}\,\mathrm{Mpc}$ give spurious results for $z < 6$. The fact that we require larger boxes for hot gas is not surprising because objects with high virial temperatures are rare and large.

The evolution of the metallicities of the different components in the two sets of simulations is shown in Fig. 3.21. Interestingly, except for the ICM, the results appear to have converged already for our smallest simulation boxes (although this is not quite true for the stellar metallicity in L006N128). Together with Fig. 3.20 this suggests that it is easier to obtain convergence for the metallicity than for the metal mass fraction. This in turn implies that the lack of convergence of the metal mass fractions for the smallest boxes was caused by non-convergence of the baryonic mass fraction rather than the metallicity.

However, part of the difference in appearance can be accounted for by the fact that

the y-axis spans six decades in Fig. 3.21, but only two decades in Fig. 3.20. Closer inspection reveals that while this explanation may be viable for the stars, it does not hold for the gaseous components. Furthermore, the axis ranges differ for a reason: they show the range of interest. While we generally do not care whether the metal mass fraction in a particular component is 10^{-3} or 10^{-2} when drawing up a census of metals (both fractions are negligible), it is very interesting to know whether the diffuse IGM has a metallicity of 10^{-3} or 10^{-2} solar because the difference is measurable and because it has important consequences for enrichment scenarios.

Finally, we plot the probability density functions of the gas density, temperature and metallicity as well as the stellar metallicity, all weighted by metal mass, in Fig. 3.22. The results confirm the conclusions drawn from the previous two figures. This figure illustrates clearly that differences first show up at the extremes of the distribution, which is not surprising since those correspond to rare objects.

Summarizing, a $50\ h^{-1}\,\mathrm{Mpc}$ box is sufficient to obtain a converged picture of the cosmic metal mass fractions and metallicities of most components down to $z = 0$. Somewhat smaller boxes may suffice if one is only interested in higher redshifts (except for the ICM, $12.5\ h^{-1}\,\mathrm{Mpc}$ is sufficient for $z > 2$) or in low-mass objects. We caution the reader that it is possible that larger box sizes are needed if other aspects of the cosmic metal distribution are investigated (e.g., clustering strengths of metal absorption lines).

3.B VARYING THE RESOLUTION

While the size of the simulation box mainly determines the types of structures that can form, numerical resolution can even have a large effect on common objects. For example, simulations that do not resolve the Jeans scales may underestimate the fraction of the mass in collapsed structures and hence the total amount of metals produced. Moreover, processes like metal mixing (see §3.6.2) may depend on resolution. To isolate the effect of numerical resolution, it is important to hold the simulation box size constant (or to use a box sufficiently large for the result to have converged with respect to the size of the simulation box).

Before showing the results of the convergence tests, it is useful to consider what to expect. The temperature of substantially overdense[14] gas does not drop much below 10^4 K in our simulations (see Fig. 3.15). In reality, gas at interstellar densities ($n_\mathrm{H} \gtrsim 10^{-1}\,\mathrm{cm}^{-3}$) is sufficiently dense and self-shielded to form a cold ($T \ll 10^4\,\mathrm{K}$), interstellar phase, allowing it to form stars (Schaye 2004). However, our simulations impose an effective equation of state for gas with densities exceeding our star formation threshold of $n_\mathrm{H} = 10^{-1}\,\mathrm{cm}^{-3}$. For our equation of state, $P \propto \rho^{4/3}$, the Jeans mass is independent of the density. Hence, provided we resolve the Jeans mass at the star formation threshold, we resolve it everywhere. The Jeans mass is given by

$$M_\mathrm{J} \approx 1 \times 10^7\,h^{-1}\,\mathrm{M}_\odot f_\mathrm{g}^{3/2} \left(\frac{n_\mathrm{H}}{10^{-1}\,\mathrm{cm}^{-3}}\right)^{-1/2} \left(\frac{T}{10^4\,\mathrm{K}}\right)^{3/2}, \tag{3.25}$$

[14]Gas with very low overdensities can have temperatures substantially below 10^4 K due to adiabatic expansion, but the Jeans scales corresponding to these low densities are nevertheless large.

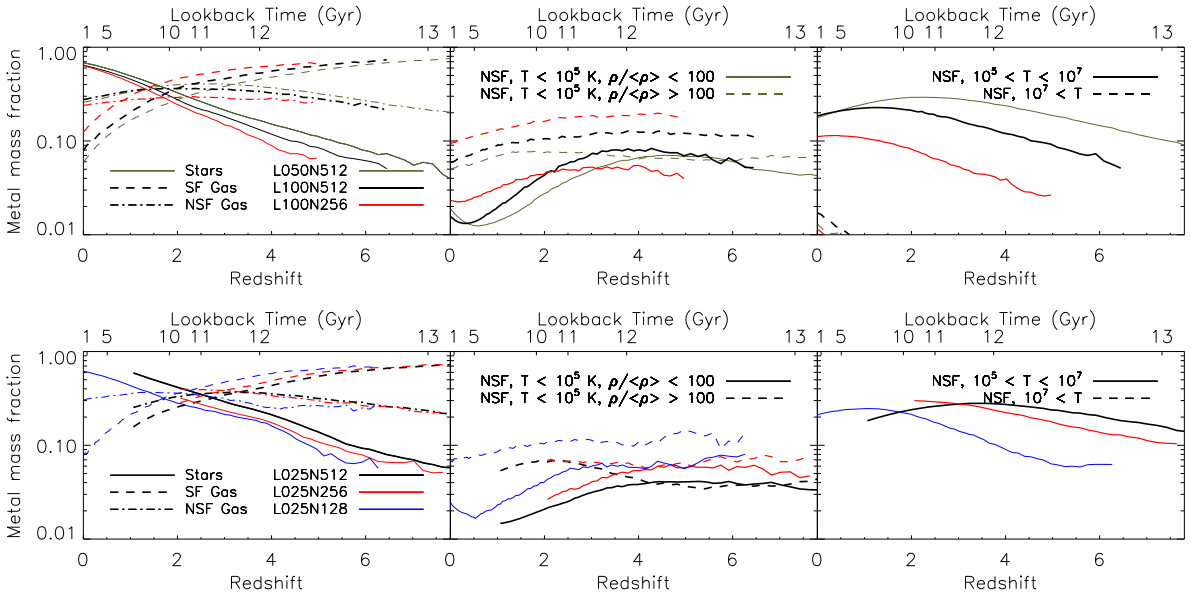

Figure 3.23: Dependence on the numerical resolution of the evolution of the fractions of the metal mass in various components. The curves in the top panels correspond to the L050N512 (olive), L100N512 (black), and the L050N256 (red) simulations. The curves in the bottom panels are for the L025N512 (black), L025N256 (red), and the L025N128 (blue) simulations. The line styles are identical to those shown in Fig. 3.13. The parts of the curves corresponding to redshifts for which the total metal is smaller than 10^{-6} of the total baryonic mass have been omitted because they become very noisy. Convergence is relatively poor for $z > 2$ in the top row and for $z > 4$ in the bottom row.

where $f_{\rm g}$ is the local gas fraction. Hence, we do not expect convergence unless the gas particle mass $m_{\rm g} \ll 10^7\,M_\odot$. To achieve convergence, a simulation will, however, also need to resolve the Jeans length $L_{\rm J}$, which implies that the maximum, proper gravitational softening, $\epsilon_{\rm prop}$, must be small compared with the Jeans Length

$$L_{\rm J} \approx 1.5\,h^{-1}\,{\rm kpc}\,f_{\rm g}^{1/2}\left(\frac{n_{\rm H}}{10^{-1}\,{\rm cm}^{-3}}\right)^{-1/2}\left(\frac{T}{10^4\,{\rm K}}\right)^{1/2}. \tag{3.26}$$

Note that since $L_{\rm J}$ scales as $L_{\rm J} \propto \rho^{-1/3}$ for our equation of state, the softening scale will always exceed $L_{\rm J}$ for sufficiently large densities. However, since the Jeans mass does not decrease with density, runaway collapse is not expected for star-forming gas. Comparing the above equations with the particle mass and softening scales listed in Table 3.2, we see that while our highest resolution simulation (L025N512) marginally resolves the Jeans scales for $f_{\rm g} \approx 1$, this is not the case for the simulations that go down to $z = 0$, although L050N512 has $m_{\rm g} \approx M_{\rm J}$ and $\epsilon_{\rm prop} \approx L_{\rm J}$ and is therefore not far off.

However, resolving the Jeans scales post-reionization may not even be sufficient, given that the simulations start at $z \gg z_{\rm reion}$. Prior to reionization the gas temperature can be much lower in which case we have no hope of resolving the Jeans scales at the threshold for star formation. On the other hand, a photo-dissociating UV background may well prevent the collapse of haloes with virial temperatures smaller than $10^4\,{\rm K}$.

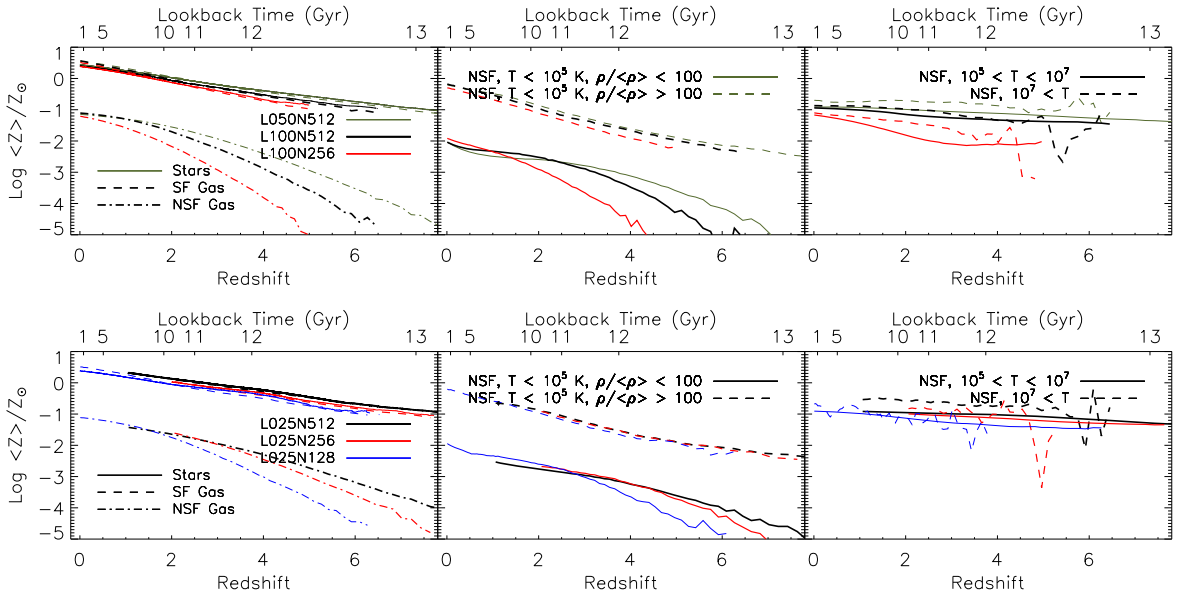

Figure 3.24: Dependence on numerical resolution of the evolution of the metallicities of various components. The colors and line styles are identical to those used in Fig. 3.23. Convergence is good for $z < 2$ in the top row and for $2 < z < 4$ in the bottom row.

In any case, we expect the duration of this period to be comparatively short. Our simulations assume $z_{\rm reion} = 9$ and include a photo-dissociating background for $z > 9$ (see §3.2). Hence, in our simulations the formation of haloes with $T_{\rm vir} \ll 10^4\,{\rm K}$ will be efficiently suppressed.

We test for convergence with resolution using two sets of simulations, which use different box sizes. The first set consists of L100N256, L100N512, and L050N512 and the second set comprises L025N128, L025N256, and L025N512. Within each set the mass (spatial) resolution is thus increased by factors of 8 and 64 (2 and 4), respectively. Note that L050N512, the highest resolution run of the first set, uses a $50\ h^{-1}\,{\rm Mpc}$ box whereas the other runs of this set used a $100\ h^{-1}\,{\rm Mpc}$ box. However, as we have shown in appendix 3.A, $50\ h^{-1}\,{\rm Mpc}$ is sufficiently large to give converged results for all phases but the ICM. We do not show L100N128 because most of its predictions are completely unreliable due to its extremely low resolution. The second set of simulations uses a box size of only $25\ h^{-1}\,{\rm Mpc}$, but these higher resolution runs were not continued down to $z = 0$.

Figures 3.23 – 3.25 are analogous to figures 3.20 – 3.22 but show the effect of varying the resolution rather than the size of the simulation box. The top row of Fig. 3.23 shows no evidence for full convergence, but the difference between L100N512 (black) and L050N512 (dark green) is small for $z < 1$. From the bottom row of panels we can see that L025N512, while certainly not fully converged, is similar to L025N256 for $z < 4$. As the resolution is increased, the fractions of the metal mass in stars and the WHIM tend to increase, while the fractions in non-star-forming gas with $T < 10^5\,{\rm K}$ tend to decrease.

It is not surprising that convergence is better at lower redshift, because the typical

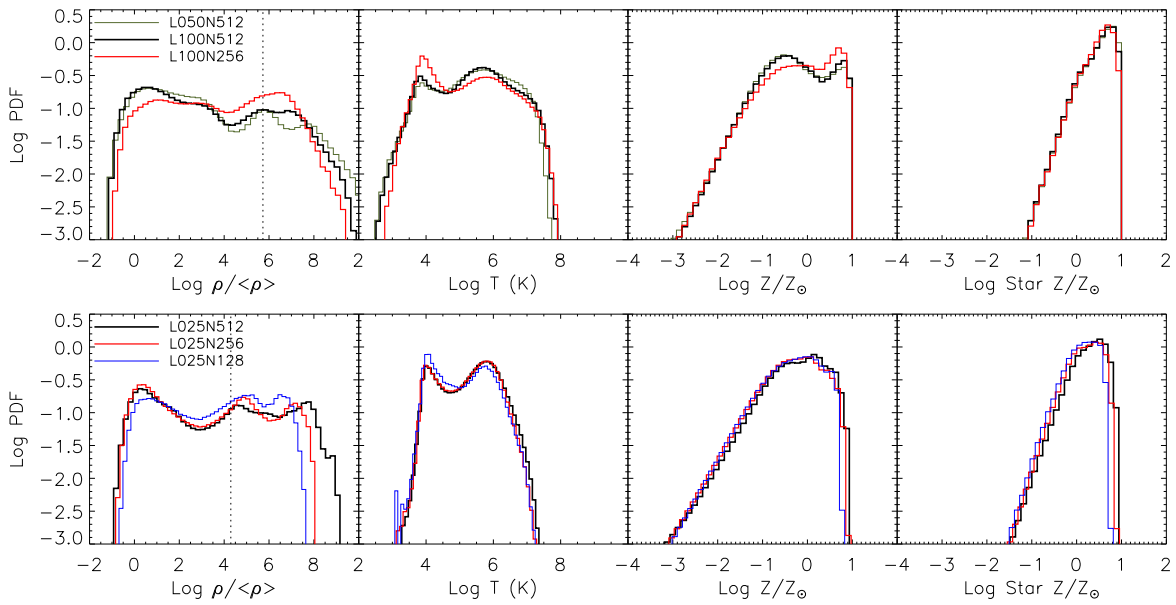

Figure 3.25: Dependence on numerical resolution of the probability density function, weighted by metal mass, of the gas density (left), temperature (centre-left), gas metallicity (centre-right), and stellar metallicity (right) at $z = 0$ (top) and $z = 2$ (bottom). The colors and line styles are identical to those used in Fig. 3.23. The vertical, dotted lines in the left panels indicate the threshold for star formation. Note that star-forming gas was excluded from the temperature panels. The highest resolution simulations have nearly converged.

mass of star-forming haloes increases with decreasing redshift which means it will be sampled with more particles per halo. In particular, lower resolution simulations will start forming stars later and it takes some time for the resultant underestimate of the metal mass to become negligible.

Figure 3.24 shows that it is much easier to get convergence for the metallicity of the different components than it is to get converged predictions for the metal mass fractions. As for convergence with box size, this partly reflects the fact that we do not require as much precision for the metallicities since the dynamic range of interest is much larger than it is for the metal mass fractions. The metallicities are nearly converged in the L050N512 run for $z < 2$ and in the L025N512 for $z < 4$. Finally, Fig. 3.25 confirms the finding from Fig. 3.23 that increasing the resolution mainly moves metals from cold-warm halo and ISM gas to the WHIM. In addition, Fig. 3.25 shows that the high-density cut-off to the gas distribution is mainly set by resolution, which is expected because many particles and small softening lengths are needed to sample the tail of the density distribution. The main conclusion we draw from this figure is, however, that the convergence is sufficiently good to draw interesting conclusions, particularly for the $25\ h^{-1}\,\mathrm{Mpc}$ box at $z = 2$ and the $50\ h^{-1}\,\mathrm{Mpc}$ box at $z = 0$.

Thus, the results of the convergence tests mostly agree with the expectations based on comparisons of the numerical resolution with the Jeans scales. The resolution of the L100N512 run ($m_g \approx 9 \times 10^7\,h^{-1}\,\mathrm{M}_\odot$) is sufficient to draw qualitative conclusions regarding the mass fractions in various phases and for $z < 2$ the L050N512

($m_g \approx 1 \times 10^7\,h^{-1}\,\mathrm{M}_\odot$) may be close to convergence. Run L100N512 already has sufficient resolution to obtain interesting, quantitative predictions for the metallicities of the different phases at $z < 2$. For $z > 2$ we need higher resolution. While the mass fractions are still not fully converged for L025N512 ($m_g \approx 1 \times 10^6\,h^{-1}\,\mathrm{M}_\odot$), its predictions for the metallicities are robust for $z < 4$.

REFERENCES

Abel T., Haehnelt M. G., 1999, ApJ, 520, L13

Aguirre A., Dow-Hygelund C., Schaye J., Theuns T., 2008, ApJ, 689, 851

Aguirre A., Schaye J., Hernquist L., Kay S., Springel V., Theuns T., 2005, ApJ, 620, L13

Allende Prieto C., Lambert D. L., Asplund M., 2001, ApJ, 556, L63

Allende Prieto C., Lambert D. L., Asplund M., 2002, ApJ, 573, L137

Alongi M., Bertelli G., Bressan A., Chiosi C., Fagotto F., Greggio L., Nasi E., 1993, Ap&SS, 97, 851

Arimoto N., Yoshii Y., 1987, A&A, 173, 23

Barris B. J., Tonry J. L., 2006, ApJ, 637, 427

Berczik P., 1999, A&A, 348, 371

Blanc G. e. a., 2004, A&A, 423, 881

Borgani S., Fabjan D., Tornatore L., Schindler S., Dolag K., Diaferio A., 2008, Space Science Reviews, 134, 379

Brachwitz F., Dean D. J., Hix W. R., Iwamoto K., Langanke K., Martínez-Pinedo G., Nomoto K., Strayer M. R., Thielemann F.-K., Umeda H., 2000, ApJ, 536, 934

Bradamante F., Matteucci F., D'Ercole A., 1998, A&A, 337, 338

Bruzual G., Charlot S., 2003, MNRAS, 344, 1000

Bryan G. L., Machacek M., Anninos P., Norman M. L., 1999, ApJ, 517, 13

Cappellaro E., Evans R., Turatto M., 1999, A&A, 351, 459

Carigi L., 2000, Revista Mexicana de Astronomia y Astrofisica, 36, 171

Carigi L., 2003, MNRAS, 339, 825

Ceverino D., Klypin A., 2007, ArXiv e-prints, 712

Chabrier G., 2003, PASP, 115, 763

Chieffi A., Domínguez I., Limongi M., Straniero O., 2001, ApJ, 554, 1159

Chieffi A., Limongi M., 2004, ApJ, 608, 405

Crowther P., Smartt S., 2007, Astronomy and Geophysics, 48, 010000

Dahlen T., Strolger L.-G., Riess A. G., Mobasher B., Chary R.-R., Conselice C. J., Ferguson H. C., Fruchter A. S., Giavalisco M., Livio M., Madau P., Panagia N., Tonry J. L., 2004, ApJ, 613, 189

Dalgarno A., McCray R. A., 1972, ARA&A, 10, 375

Dalla Vecchia C., Schaye J., 2008, MNRAS, 387, 1431

Davé R., Oppenheimer B. D., 2007, MNRAS, 374, 427

David L. P., Forman W., Jones C., 1990, ApJ, 359, 29

de Avillez M. A., Breitschwerdt D., 2007, ApJ, 665, L35

Della Valle M., Panagia N., Padovani P., Cappellaro E., Mannucci F., Turatto M., 2005, ApJ, 629, 750

Erb D. K., Shapley A. E., Pettini M., Steidel C. C., Reddy N. A., Adelberger K. L., 2006, ApJ, 644, 813

Fechner C., Richter P., 2008, ArXiv e-prints

Ferland G. J., Korista K. T., Verner D. A., Ferguson J. W., Kingdon J. B., Verner E. M., 1998, PASP, 110, 761

Forestini M., Charbonnel C., 1997, Ap&SS, 123, 241

Förster F., Wolf C., Podsiadlowski P., Han Z., 2006, MNRAS, 368, 1893

François P., Matteucci F., Cayrel R., Spite M., Spite F., Chiappini C., 2004, A&A, 421, 613

Gallazzi A., Brinchmann J., Charlot S., White S. D. M., 2008, MNRAS, 383, 1439

Gavilán M., Buell J. F., Mollá M., 2005, A&A, 432, 861

Goswami A., Prantzos N., 2000, A&A, 359, 191

Governato F., Willman B., Mayer L., Brooks A., Stinson G., Valenzuela O., Wadsley J., Quinn T., 2007, MNRAS, 374, 1479

Greggio L., Renzini A., 1983, A&A, 118, 217

Greif T. H., Glover S. C. O., Bromm V., Klessen R. S., 2008, ArXiv e-prints

Haardt F., Madau P., 2001, in Neumann D. M., Tran J. T. V., eds, Clusters of Galaxies and the High Redshift Universe Observed in X-rays Modelling the UV/X-ray cosmic background with CUBA

Hachisu I., Kato M., Nomoto K., 1999, ApJ, 522, 487

Halliday C., Daddi E., Cimatti A., Kurk J., Renzini A., Mignoli M., Bolzonella M., Pozzetti L., Dickinson M., Zamorani G., Berta S., Franceschini A., Cassata P., Rodighiero G., Rosati P., 2008, A&A, 479, 417

Hardin D. e. a., 2000, A&A, 362, 419

Hirschi R., Meynet G., Maeder A., 2005, A&A, 433, 1013

Holweger H., 2001, in Wimmer-Schweingruber R. F., ed., Joint SOHO/ACE workshop "Solar and Galactic Composition" Vol. 598 of American Institute of Physics Conference Series, Photospheric Abundances: Problems, Updates, Implications. pp 23–+

Hui L., Gnedin N. Y., 1997, MNRAS, 292, 27

Iben I., Truran J. W., 1978, ApJ, 220, 980

Iwamoto K., Brachwitz F., Nomoto K., Kishimoto N., Umeda H., Hix W. R., Thielemann F.-K., 1999, ApJS, 125, 439

Izzard R. G., Tout C. A., Karakas A. I., Pols O. R., 2004, MNRAS, 350, 407

Karakas A. I., Lattanzio J. C., Pols O. R., 2002, Publications of the Astronomical Society of Australia, 19, 515

Kawata D., 1999, PASJ, 51, 931

Kawata D., 2001, ApJ, 558, 598

Kawata D., Gibson B. K., 2003, MNRAS, 346, 135

Kennicutt Jr. R. C., 1998, ApJ, 498, 541

Kippenhahn R. W. A., Weigert A., 1994, Stellar Structure and Evolution. Stellar Structure and Evolution, XVI, 468 pp. 192 figs.. Springer-Verlag Berlin Heidelberg New York. Also Astronomy and Astrophysics Library

Kobayashi C., 2004a, MNRAS, 347, 740

Kobayashi C., 2004b, MNRAS, 347, 740

Kobayashi C., Springel V., White S. D. M., 2007, MNRAS, 376, 1465

Kobayashi C., Tsujimoto T., Nomoto K., 2000, ApJ, 539, 26

Kodama T., 1997, Ph.D. Thesis

Komatsu E., Dunkley J., Nolta M. R., Bennett C. L., Gold B., Hinshaw G., Jarosik N., Larson D., Limon M., Page L., Spergel D. N., Halpern M., Hill R. S., Kogut A., Meyer S. S., Tucker G. S., Weiland J. L., Wollack E., Wright E. L., 2008, ArXiv e-prints, 803

Kroupa P., Tout C. A., Gilmore G., 1993, MNRAS, 262, 545

Kuznetsova N., Barbary K., Connolly B., Kim A. G., Pain R., Roe N. A., Aldering G., Amanullah R., Dawson K., Doi M., Fadeyev V., Fruchter A. S., Gibbons R., Goldhaber G., Goobar A., Gude A., 2008, ApJ, 673, 981

Lia C., Portinari L., Carraro G., 2002, MNRAS, 330, 821

Liang Y. C., Zhao G., Shi J. R., 2001, A&A, 374, 936

Lindner U., Fritze-v. Alvensleben U., Fricke K. J., 1999, A&A, 341, 709

Madgwick D. S., Hewett P. C., Mortlock D. J., Wang L., 2003, ApJL, 599, L33

Maeder A., 1987, A&A, 173, 247

Maeder A., 1992, A&A, 264, 105

Maeder A., Meynet G., 1989a, A&A, 210, 155

Maeder A., Meynet G., 1989b, A&A, 210, 155

Mannucci F., Della Valle M., Panagia N., 2006, MNRAS, 370, 773

Mannucci F., Della Valle M., Panagia N., Cappellaro E., Cresci G., Maiolino R., Petrosian A., Turatto M., 2005, A&A, 433, 807

Marigo P., 2001, A&A, 370, 194

Matteucci F., 2001, Nature, 414, 253

McCarthy I. G., Schaye J., Ponman T. J., Bower R. G., Booth C. M., Dalla Vecchia C., Crain R. A., Springel V., Theuns T., Wiersma R. P. C., 2009, ArXiv e-prints

Miller G. E., Scalo J. M., 1979, ApJS, 41, 513

Mori M., Umemura M., 2006, Nature, 440, 644

Mosconi M. B., Tissera P. B., Lambas D. G., Cora S. A., 2001, MNRAS, 325, 34

Nagashima M., Lacey C. G., Baugh C. M., Frenk C. S., Cole S., 2005, MNRAS, 358, 1247

Navarro J. F., White S. D. M., 1993, MNRAS, 265, 271

Neill J. D. e. a., 2006, AJ, 132, 1126

Nomoto K., Hashimoto M., Tsujimoto T., Thielemann F.-K., Kishimoto N., Kubo Y., Nakasato N., 1997, Nuclear Physics A, 616, 79

Nomoto K., Iwamoto K., Kishimoto N., 1997, Science, 276, 1378

Nomoto K., Iwamoto K., Nakasato N., Thielemann F.-K., Brachwitz F., Tsujimoto T., Kubo Y., Kishimoto N., 1997, Nuclear Physics A, 621, 467

Nomoto K., Thielemann F.-K., Yokoi K., 1984, ApJ, 286, 644

Nomoto K., Tominaga N., Umeda H., Kobayashi C., Maeda K., 2006, Nuclear Physics A, 777, 424

Nykytyuk T. V., Mishenina T. V., 2006, A&A, 456, 969

Okamoto T., Eke V. R., Frenk C. S., Jenkins A., 2005, MNRAS, 363, 1299

Oppenheimer B. D., Davé R., 2006, MNRAS, 373, 1265

Oppenheimer B. D., Davé R., 2008, MNRAS, 387, 577

Padovani P., Matteucci F., 1993, ApJ, 416, 26

Pain R. e. a., 2002, ApJ, 577, 120

Pawlik A. H., Schaye J., 2008, MNRAS, 389, 651

Pearce F. R., Jenkins A., Frenk C. S., Colberg J. M., White S. D. M., Thomas P. A., Couchman H. M. P., Peacock J. A., Efstathiou G., The Virgo Consortium 1999, ApJ, 521, L99

Podsiadlowski P., Mazzali P., Lesaffre P., Han Z., Förster F., 2008, New Astronomy Review, 52, 381

Portinari L., Chiosi C., Bressan A., 1998, A&A, 334, 505

Portinari L., Moretti A., Chiosi C., Sommer-Larsen J., 2004, ApJ, 604, 579

Poznanski D., Maoz D., Yasuda N., Foley R. J., Doi M., Filippenko A. V., Fukugita M., Gal-Yam A., Jannuzi B. T., Morokuma T., Oda T., Schweiker H., Sharon K., Silverman J. M., Totani T., 2007, MNRAS, 382, 1169

Prochaska J. X., Gawiser E., Wolfe A. M., Castro S., Djorgovski S. G., 2003, ApJL, 595, L9

Raiteri C. M., Villata M., Navarro J. F., 1996, A&A, 315, 105

Rauscher T., Heger A., Hoffman R. D., Woosley S. E., 2002, ApJ, 576, 323

Recchi S., Matteucci F., D'Ercole A., 2001, MNRAS, 322, 800

Renzini A., Voli M., 1981, A&A, 94, 175

Ricotti M., Gnedin N. Y., Shull J. M., 2000, ApJ, 534, 41

Romano D., Chiappini C., Matteucci F., Tosi M., 2005, A&A, 430, 491

Romeo A. D., Sommer-Larsen J., Portinari L., Antonuccio-Delogu V., 2006, MNRAS, 371, 548

Salpeter E. E., 1955, ApJ, 121, 161

Scannapieco C., Tissera P. B., White S. D. M., Springel V., 2005, MNRAS, 364, 552

Scannapieco E., Bildsten L., 2005a, ApJL, 629, L85

Scannapieco E., Bildsten L., 2005b, ApJ, 629, L85

Schaye J., 2004, ApJ, 609, 667

Schaye J., Aguirre A., Kim T.-S., Theuns T., Rauch M., Sargent W. L. W., 2003, ApJ, 596, 768

Schaye J., Dalla Vecchia C., 2008, MNRAS, 383, 1210

Schaye J., Dalla Vecchia C., Booth C. M., Wiersma R. P. C., Theuns T., Haas M. R., Bertone S., Duffy A. R., McCarthy I. G., van de Voort F., 2009, ArXiv e-prints

Schaye J., Theuns T., Rauch M., Efstathiou G., Sargent W. L. W., 2000, MNRAS, 318, 817

Seljak U., Zaldarriaga M., 1996, ApJ, 469, 437

Simionescu A., Werner N., Böhringer H., Kaastra J. S., Finoguenov A., Brüggen M., Nulsen P. E. J., 2009, A&A, 493, 409

Sommer-Larsen J., Romeo A. D., Portinari L., 2005, MNRAS, 357, 478

Springel V., 2005, MNRAS, 364, 1105

Springel V., Hernquist L., 2003, MNRAS, 339, 289

Steinmetz M., Mueller E., 1994, A&A, 281, L97

Steinmetz M., Muller E., 1995, MNRAS, 276, 549

Stinson G., Seth A., Katz N., Wadsley J., Governato F., Quinn T., 2006, MNRAS, 373, 1074

Sutherland R. S., Dopita M. A., 1993, ApJS, 88, 253

Theis C., Burkert A., Hensler G., 1992, A&A, 265, 465

Theuns T., Leonard A., Efstathiou G., Pearce F. R., Thomas P. A., 1998, MNRAS, 301, 478

Theuns T., Leonard A., Schaye J., Efstathiou G., 1999, MNRAS, 303, L58

Theuns T., Viel M., Kay S., Schaye J., Carswell R. F., Tzanavaris P., 2002, ApJ, 578, L5

Thielemann F.-K., Argast D., Brachwitz F., Hix W. R., Höflich P., Liebendörfer M., Martinez-Pinedo G., Mezzacappa A., Nomoto K., Panov I., 2003, in From Twilight to Highlight: The Physics of Supernovae Supernova Nucleosynthesis and Galactic Evolution. pp 331–+

Thielemann F.-K., Nomoto K., Hashimoto M., 1993, in Origin and Evolution of the Elements . pp 299–+

Timmes F. X., Woosley S. E., Weaver T. A., 1995, ApJS, 98, 617

Tonry J. L. e. a., 2003, ApJ, 594, 1

Tornatore L., Borgani S., Dolag K., Matteucci F., 2007, MNRAS, 382, 1050

Tornatore L., Borgani S., Matteucci F., Recchi S., Tozzi P., 2004, MNRAS, 349, L19

Travaglio C., Hillebrandt W., Reinecke M., Thielemann F.-K., 2004, A&A, 425, 1029

Tsujimoto T., Nomoto K., Yoshii Y., Hashimoto M., Yanagida S., Thielemann F.-K., 1995, MNRAS, 277, 945

Valdarnini R., 2003, MNRAS, 339, 1117

van den Hoek L. B., Groenewegen M. A. T., 1997, Ap&SS, 123, 305

Veilleux S., Cecil G., Bland-Hawthorn J., 2005, ARA&A, 43, 769

Wanajo S., Nomoto K., Janka H. ., Kitaura F. S., Mueller B., 2008, ArXiv e-prints

White S. D. M., 1994, ArXiv Astrophysics e-prints

Woosley S. E., Weaver T. A., 1995, ApJS, 101, 181